

## **Assessment of North Slope of Alaska (NSA) Snow Monitoring Arrays**

M Sturm  
J Delamere

WH Barndt  
K Irving

May 2025



## **DISCLAIMER**

This report was prepared as an account of work sponsored by the U.S. Government. Neither the United States nor any agency thereof, nor any of their employees, makes any warranty, express or implied, or assumes any legal liability or responsibility for the accuracy, completeness, or usefulness of any information, apparatus, product, or process disclosed, or represents that its use would not infringe privately owned rights. Reference herein to any specific commercial product, process, or service by trade name, trademark, manufacturer, or otherwise, does not necessarily constitute or imply its endorsement, recommendation, or favoring by the U.S. Government or any agency thereof. The views and opinions of authors expressed herein do not necessarily state or reflect those of the U.S. Government or any agency thereof.

# **Assessment of North Slope of Alaska (NSA) Snow Monitoring Arrays**

M Sturm  
WH Barndt  
J Delamere  
K Irving  
All at Geophysical Institute, University of Alaska Fairbanks

May 2025

How to cite this document:

Sturm, M, WH Barndt, J Delamere, and K Irving. Assessment of North Slope of Alaska (NSA) Snow Monitoring Arrays. 2025. U.S. Department of Energy, Atmospheric Radiation Measurement User Facility, Richland, Washington. DOE/SC-ARM-24-025.

Work supported by the U.S. Department of Energy,  
Office of Science, Office of Biological and Environmental Research

## **Executive Summary**

Arrays of instruments for monitoring winter precipitation (snowfall) and snow cover on the ground installed in 2017 at the U.S. Department of Energy Atmospheric Radiation Measurement (ARM) user facility's North Slope of Alaska (NSA) C1 and at Oliktok Point sites became operational in 2018. In 2022, the instruments from Oliktok Point were moved to NSA E12, about 5.4 km south of NSA C1, where two arrays now operate. The instrument arrays monitor wind speed and direction, snow depth at multiple locations, the horizontal flux of blowing snow, and the number and fall speed of hydrometeors. The arrays are monitored using digital cameras. Collectively, the instruments produce a wealth of data on falling and accumulated snow, but, as with any instrument array, some data are more reliable and accurate than others. In this document, we present our findings on the efficacy, accuracy, and reliability of each type of instrument. Overall, a key finding is that no single instrument provides sufficient information to determine the source of falling snow particles nor the cause of changes in snow depth. However, if used in concert, the instruments produce a reliable understanding of the processes affecting the snow cover depth distribution and the true winter precipitation.

More specifically, we find that:

- Using a single snow depth (e.g., derived from a snow depth sounder) can be greatly misleading. We recommend using depth averages from the full C1 and E12 arrays and being aware that snow depth is tied closely to the local meso- and micro-topography surrounding the sites as well as the accumulated precipitation.
- The current instruments that measure the horizontal flux of blowing snow are excellent for identifying when such events occur and their relative intensity. However, for several reasons, they tend to underreport the total blowing flux, especially during periods of snow and wind.
- In principle, automated computer routines could be developed that integrate the data streams from the multiple instruments at C1 and E12, making the ensemble result more reliable and accurate. Such an integrated product would provide a more nuanced understanding of the winter precipitation regime and the snow cover at C1 and E12.

## **Acknowledgments**

Many people have helped ensure that the snow monitoring instruments at the ARM NSA C1, E12, and Oliktok Point sites operated well. First, we thank Drs. Mark Ivey and Jim Mather for deciding that snow was important to monitor in the ARM system. Second, we thank Walter Brower, Jimmy Ivanoff, and Josh Ivanoff at ARM NSA for years of assistance, including going out in cold winter conditions to fix things when we called them from Fairbanks. Fred Helsel, Valerie Sparks, Ben Bishop, Justin LaPierre, and Andy Glen have been essential in keeping the instruments operating. Telayna Wong has been a source of valuable advice and assistance. Ross Burgener and Brian Thomas at the National Oceanic and Atmospheric Administration (NOAA) station have supported this work in numerous ways.

## Acronyms and Abbreviations

2D	two-dimensional
3D	three-dimensional
ARM	Atmospheric Radiation Measurement
CV	coefficient of variation (standard deviation divided by the mean: $\sigma / \mu$ )
DFIR	Double Fence Intercomparison Reference
GML	Global Monitoring Laboratory
LPM	laser precipitation monitor
NaN	Not-a-number
NARL	Naval Arctic Research Laboratory
NetCDF	Network Common Data Form
NOAA	National Oceanic and Atmospheric Administration
NSA	North Slope of Alaska
PVC	polyvinyl chloride
PWS	present weather sensor
SONICWIND3D	ultrasonic 3D anemometer
SPMF	solid particles mass flux sensor
SRS	sonic ranging sounder
UDS	ultrasonic depth sensor
U3D	ultrasonic 3D anemometer (synonym for SONICWIND3D)
WBGEONOR	weighing bucket Geonor totalizing precipitation gauge

## Contents

Executive Summary .....	iii
Acknowledgments.....	iv
Acronyms and Abbreviations .....	v
1.0 Introduction .....	1
2.0 Snow Depth .....	3
2.1 The Impact of Micro- and Meso-Topography on Snow Depth.....	8
2.2 Data Quality Variable.....	10
3.0 Wind .....	13
4.0 Blowing Snow .....	15
4.1 Mechanisms of Snow Transport.....	17
4.2 SPMF Wind Speed.....	18
4.3 SPMF Flux Measurements.....	19
5.0 Totalizing Precipitation Gauge (WBGEONOR or Geonor).....	21
6.0 Falling Snow and Rain .....	22
6.1 Examples of LPM Events.....	27
6.2 Particle Count Comparisons of C1 and E10 LPMs.....	32
6.3 Comparing C1 and E12 .....	33
7.0 Using Multi-Instrument Ensemble Data to Better Understand the Snow Cover Evolution .....	35
8.0 Conclusions .....	36
9.0 References .....	37
Appendix A – Modifications of Data Prior to Ingest (A1) Level .....	A.1
Appendix B – “A1+”-Level Data Processing .....	B.1

## Figures

1 The locations of C1 and E12 snow monitoring arrays. NARL is the Naval Arctic Research Laboratory. ....	1
2 The snow depth on the tundra (G) arises from four processes, all of which vary in time and space: S (sublimation), C (condensation), T (transport), and P (precipitation). ....	2
3 The snow monitoring array at NSA C1. The array at E12 is similar.....	3
4 In the foreground are three SR50s (SRS); to their left are three white Judds (UDS), and in the rear three more Judds can just be seen. ....	5
5 Converting sonic sounder raw values to a clean snow depth record. ....	5
6 Snow depth from the nine sonic sounders at C1, 2018 to 2023. ....	6

7	Panel A: A depth transect measured adjacent to the C1 sonic sounder array on May 16, 2019, showing the extreme depth heterogeneity at the site.....	7
8	Panel A: A depth sounder record following the deposition of fluffy new snow.....	8
9	A snow event from the 2022-2023 winter illustrating local scour and fill within the sounder array.....	9
10	(Top) Elevation cross-section along red dashed line in the bottom panel with vertical exaggeration. (Bottom) Elevation map of the C1 swing sets. Blue areas are ice wedge troughs.....	9
11	The winter of 2023-2024 produced the same divergent behavior in depth across the sounder array because the divergence is driven by the fixed micro-topography of the tundra.....	10
12	Top: Snow depth for the winter of 2021-2022, color-coded by measurement date. Bottom: Quality measurements for the same data using the same color-coding.....	11
13	An example of unfiltered depth data (red dots) overlain by only data with quality values between 152 and 210 (blue dots).....	12
14	Data quality values as a function of wind speed (top) and drift flux (bottom).....	12
15	Thies-Clima three-dimensional sonic anemometer (SONICWIND3D).....	13
16	Minimum and maximum wind speeds for 2022-2023 at C1.....	14
17	Wind rose for C1 from the winter of 2022-2023.....	14
18	Vertical wind speed ( $w$ ) as a function of the horizontal wind speed.....	15
19	Upper and lower FlowCapt units (SPMFs), seen here facing into the prevailing E and NE winds.....	16
20	Three modes of wind transport of snow.....	17
21	SPMF versus sonic anemometer (U3D) wind speeds.....	19
22	An example of SPMF flux data: upper (blue) and lower (gold) SPMF mean values.....	19
23	SPMF lower sensor snow flux as a function of U3D wind speed.....	20
24	The drift flux at C1 as measured by the SPMFs (gold circles) compared to the drift flux observed at other comparable snowy locations (black diamonds).....	20
25	Comparison of the Cake Eater snow fence and the C1 SPMFs.....	21
26	Comparison of the E12 Geonor totalizing precipitation gauge with the C1 accumulated precipitation from the LPM.....	22
27	The C1 unshielded LPM.....	22
28	Raindrops at terminal velocity.....	24
29	The Gunn-Kinzer curve for raindrops falling at terminal velocity.....	24
30	Mass as a function of particle diameter and crystal type from Vázquez-Martín et al.....	25
31	From Fehlmann et al. (2020), a functional relationship between maximum horizontal diameter ( $D$ ) and particle density for snow ( $\rho$ ).....	26
32	The LPM event of January 1, 2023.....	27
33	C1 LPM total counts versus E10 total counts for the January 1 event.....	28
34	C1 (shielded) and E10 (unshielded) LPM intensity responses to the mixed-phase event on August 5, 2022, which was quite brief.....	29

35 Particle counts, C1 and E10, during the August 5 event. .... 30

36 The distribution of particles by size and fall speed for the August 5 event (contours are of total counts) shows similar values. .... 30

37 February 25 event: the intensity rises with the wind speed and is the same for C1 (green) and E10 (blue). .... 31

38 Particle distribution curves plotted by diameter and bin number ..... 31

39 Snow erosion under the sonic sounders during the February 24-25, 2023, event. .... 32

40 Comparison of the E10 and C1 LPM hydrometeor counts for the winter of 2023..... 33

41 Same as above but for the 2022 winter. .... 33

42 Accumulated winter precipitation for C1 (green) and E12 (black) showing significantly more precipitation at C1. .... 34

43 LPM intensities (bottom panel) and wind speeds (top) for C1 (green) and E12 (black)..... 34

44 The drift flux from the SPMFs at C1 (green) and E12 (black)..... 35

45 Flow chart suggesting how reliability of LPM data might be assessed..... 36

46 A simpler version of Figure 45 that might lend itself to easier implementation in code..... 36

47 Flow chart of our A1+ data processing. ....B.1

## Tables

1 SRS data quality ranges..... 10

2 (Tabler 1994): Vertical fraction of snow transport as a function of wind speed.\* ..... 18

3 Snowball sizes due to 24 hours of drift flux. .... 18

4 LPM disdrometer size and fall speed classes. .... 23

5 Correction factors for LPM size bins ..... 26

6 August 5, 2022 event LPM number counts ..... 29

7 Wind, snowfall, and drift conditions at C1 and E12. .... 35

## 1.0 Introduction

This document describes the winter precipitation monitoring arrays operating at ARM’s NSA observatory, discusses the strengths and weaknesses of each type of instrument (performance and accuracy) in the arrays, and suggests how the instruments could be used in concert to gain a more comprehensive understanding of the evolving snow conditions at each site. Handbooks for individual instruments are available and should be referred to for technical details on principles of operation, data formats, instrument heritage and maintenance, and data archiving.

Currently, two arrays of snow-monitoring instruments are installed near Utqiagvik (formerly Barrow), Alaska, as part of ARM NSA: the C1 site near the main ARM instrumentation and the E12 site, located 5.4 km south along Cake Eater Road (Figure 1). The latter set of instruments was originally operated at Oliktok Point from April 2017 to June 2021 before being relocated to E12.



**Figure 1.** The locations of C1 and E12 snow monitoring arrays. NARL is the Naval Arctic Research Laboratory.

The concept behind both monitoring arrays is that no single instrument can provide a foolproof measurement of winter precipitation and snow depth in the Arctic, where blowing snow is constant, along with instrument riming and diamond dust events. The winter mass balance (defined as *snow depth on the ground* = *snowfall* ± *transported snow* ± *sublimation/condensation*) represents the algebraic sum of four processes that vary temporally and spatially. To fully understand the end result, data related to each process (whether concerning snow cover state or winter precipitation) must be combined (see Figure 2).

The operation of two arrays—one very close to the ocean and the other 5 km inland—aims to identify gradients in weather and winter precipitation across the Barrow Peninsula.

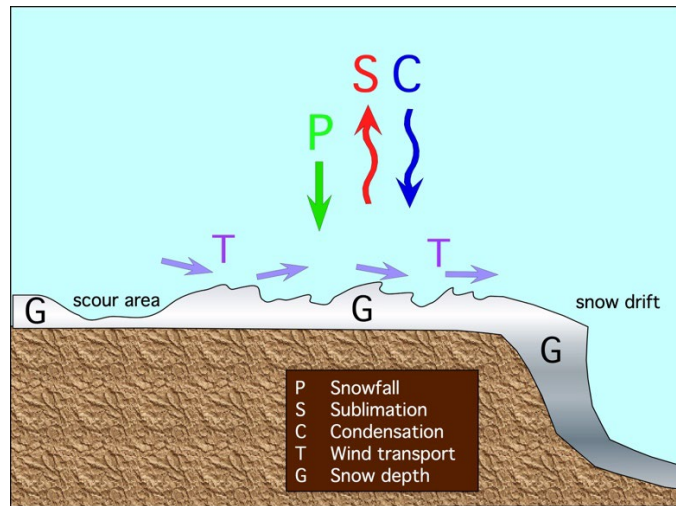


**Figure 2.** The snow depth on the tundra (G) arises from four processes, all of which vary in time and space: S (sublimation), C (condensation), T (transport), and P (precipitation).

Figure 1 shows the location of C1 and E12, and Figure 3 is an aerial view of the C1 array with a listing of the instruments in operation. The E12 array has a similar configuration. The C1 array consists of nine sonic sounders that measure the snow depth on the tundra once a minute (SRS and UDS), two stacked instruments that measure the horizontal flux of blowing snow every 10 seconds (SPMF), two instruments that measure the flux of snow falling from the sky every minute (LPM), and a heated high-speed 3D anemometer that measures the wind every 10 seconds (SONICWIND3D). Both sites also include steerable cameras that provide video images of the site every hour, with additional camera images available from cameras operated at C1 at the top of the 40-m tower. Adjacent to the C1 array, NOAA operates a totalizing precipitation gauge (Geonor: <https://www.geonor.com/t-200b-all-weather-precipitation---rain-gauge>) shielded by a Double Fence Intercomparison Reference (DFIR) fence, which at last inspection, was somewhat in disrepair, so the quality of the Geonor values from the site is not known. At E12, in addition to the instruments described for C1, we also operate a heated Geonor totalizing precipitation gauge (WBGEONOR) surrounded by a double Alter shield that measures every 10 seconds.

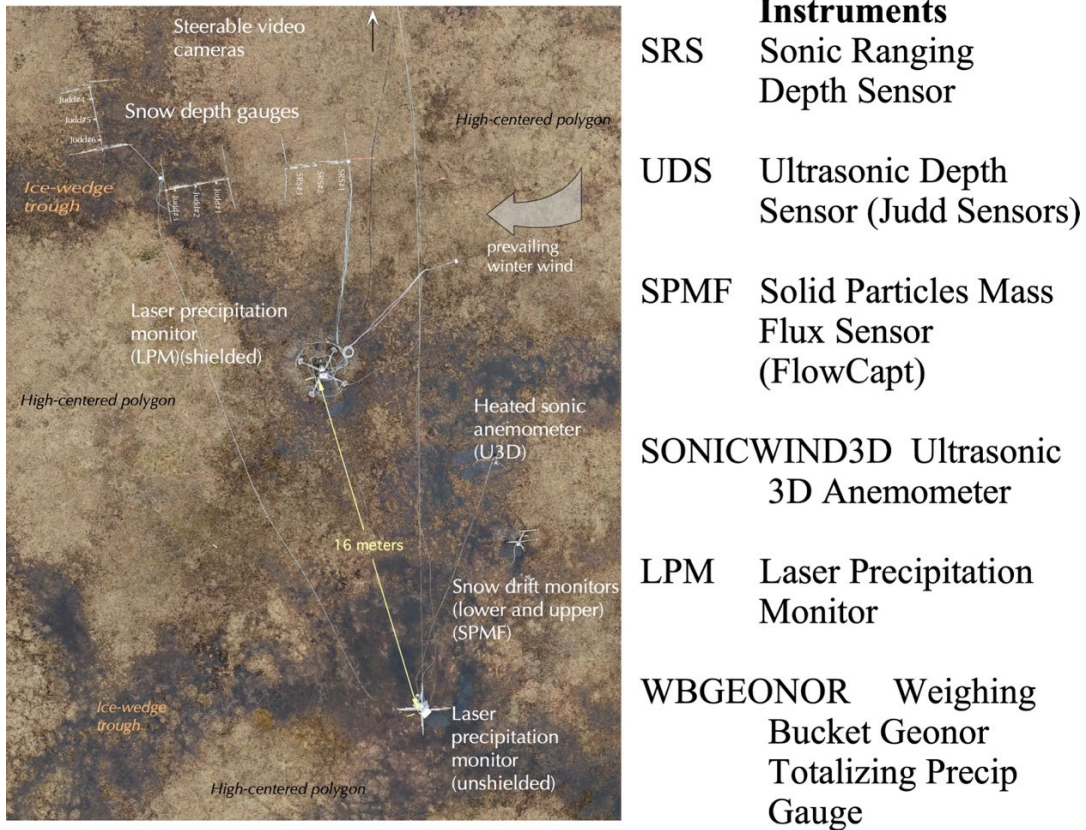


**Figure 3.** The snow monitoring array at NSA C1. The array at E12 is similar.

The ground at both the C1 and E12 sites consists of high-centered polygonal tundra with tussocks and hummocks that produce up to 25 cm of local relief. For deeper snowpacks, this would not matter, but the tundra snow near Utqiagvik averages ~50 cm at maximum depth, so the mid-winter depth distribution at horizontal scales of meters can be extremely heterogeneous, with the local micro- and meso-topography impacting the local depth. Typically, greater depths are found in ice wedge troughs versus polygon tops due to the constant scour of wind with drift deposition in hollows. Of the nine snow depth sensors at C1, three overlie a trough, three overlie a polygon top, and three are in mixed terrain. We will make the case below that, because of this local heterogeneity, a single snow depth is not a useful value without also citing the local depth variations, or even more usefully, some measure of the depth heterogeneity at scales relevant to the geophysical problem being investigated.

The arrays at C1 and E12 produce a voluminous amount of data: about 86 MBytes/week (without counting the camera imagery), so collection, ingest into the ARM Data Center, and subsequent analysis of the array sensor data is complex and time consuming. In what follows, we define the snow year as running from August 1 at midnight (00:00:00) to July 31 in the following calendar year.

## 2.0 Snow Depth

We operated two types of sonic depth sounders through 2023: Judds (UDS) (<http://juddcom.com/>) and Campbell SR50s (SRS) (<https://www.campbellsci.com/sr50>). In 2024, we replaced the Judds with Campbell SRSs. In all cases, these were (and are) mounted on pipe structures that we call swing sets

because they look like swing frames (Figure 4). The winter environment is so rigorous at the two arrays that we have routinely “lost” data from one or more sensors during the winter for various reasons. In the case of the SR50s, an essential gold foil oscillator needed to “ping” the distance to the snow becomes pitted from blowing snow, rime, and ambient salts in the air, causing the sounder to fail, sometimes in as little as a few months. We also lose depth signals from both types of sounders during heavy riming events, though when the rime is removed or falls off, a usable signal returns. We have experimented with heated and unheated sounders, developed several easy-on-off mounting systems, and varied how we plug the units into the power and signal harnesses because of the need for mid-winter sensor change-outs, but maintaining 18 sounders in operation through an arctic winter remains a challenge.

The principle of the sonic sounders is that the device pings and then measures the time for the echo to return. The down-and-back delay is then used to compute the distance to the top of the snow using the speed of sound in air ([https://www.campbellsci.com/manuals?gad\\_source=1](https://www.campbellsci.com/manuals?gad_source=1)). The formula to compute snow depth from the measured standoff distance is:

$$H_s = H_T(\text{no snow}) - H_T(i) \quad [1]$$

where  $H_s$  is the snow depth,  $H_T(\text{no snow})$  is the average standoff distance (distance to the surface before winter when there is no snow on the ground), and  $H_T(i)$  is the  $i^{\text{th}}$  reading in the time series once there is snow.

Setting the *no-snow* standoff value ( $H_T(\text{no snow})$ ) for each sonic sounder is something of an art. The sonic signal from the sensors produces a  $30^\circ$  cone such that a sensor mounted 1.5 m above the ground reports depth from a circle about 0.78 m in diameter at the ground level. In tussock tundra, that circle can easily span several tussocks with 15 to 25 cm of relief, so the reading with no snow is noisy from the sensor and difficult to define in the field using a ruler. The procedure we have found most effective is to digitally offset the depth reading with no snow (e.g., using the August signal) up or down until the majority of the time data from the pre-snow period are vertically centered on zero depth. At the end of the winter (e.g., July), following snow melt, this vertical offset can be checked against the value for no snow from the pre-snow melt period for consistency. In most cases, we find the initial *no-snow* offset remains valid throughout the winter within a few centimeters.

The speed of sound ( $V_s$ ) varies with air temperature at about  $0.6 \text{ m s}^{-1}$  per degree C. The correction for temperature is:  $V_s = 331 \text{ m s}^{-1} + (0.6 \text{ m s}^{-1} \text{ }^\circ\text{C}^{-1}) \times \Delta T$ , where  $\Delta T$  is the change from the reference temperature ( $0^\circ\text{C}$ ). We correct the temperature readings, but even if we did not, the correction would be small: at the height the sensors are mounted (about 1.5 m above the snow), a  $20^\circ\text{C}$  error in air temperature would only result in a 0.04-m shift in the reading. This speed-of-sound correction is automatic for the Judd sounders (which have an internal thermistor recording temperature) and is done for the SRSs during the ingest to the ARM Data Center using temperature data from air temperature instruments adjacent to the sounders that we operate at each site.

The sounder data are quite noisy (noise is often generated during blowing snow events), with spurious high and low depths, so once the no-snow zero is set for each sounder and Equation [1] executed for each time step, the depth data should be cleaned after downloading it from the ARM Data Center. In the analysis we report here, we have applied an upper and lower threshold to the data, removing spurious data. These thresholds are easy to identify visually on a plot of snow depth versus time because these

spikes tend to be singular and to lie either well below or well above the obvious snow depth trace. This removal process introduces *NaNs* into the record, which we then fill using a backward-looking algorithm: the  $i^{th}$  *NaN* is replaced with the last good reading ( $i-1$ ; Figure 5). We have also experimented with various smoothing algorithms to improve the signal clarity; a simple moving average smoothing using 60 data points (e.g., hourly smoothing) works well. It should be borne in mind that the native depth data filed in the ARM Data Center are for one-minute intervals, but snow depth rarely changes much in one minute; hence, smoothing can be used to produce a more usable and interpretable depth product.

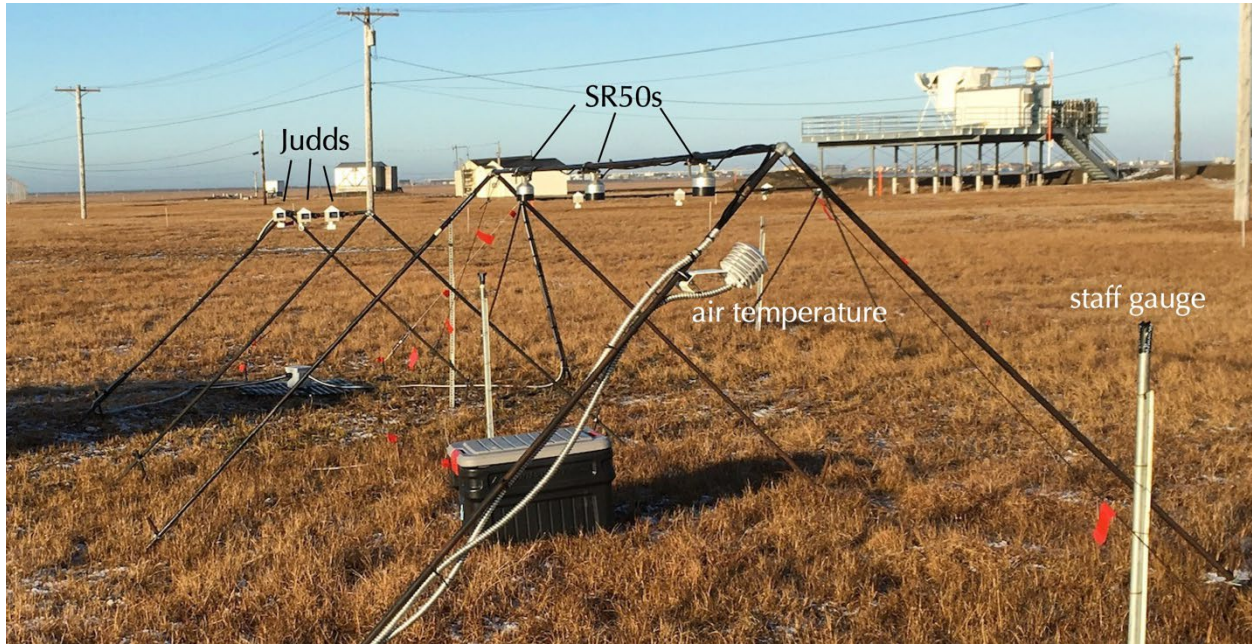


**Figure 4.** In the foreground are three SR50s (SRS); to their left are three white Judds (UDS), and in the rear three more Judds can just be seen. The sounders are spaced 1 m apart along each swing set. A staff gauge facing a video camera can be seen in the lower right. It appears in the video images taken from the main ARM C1 facility and can be used to check the sounder snow depths.

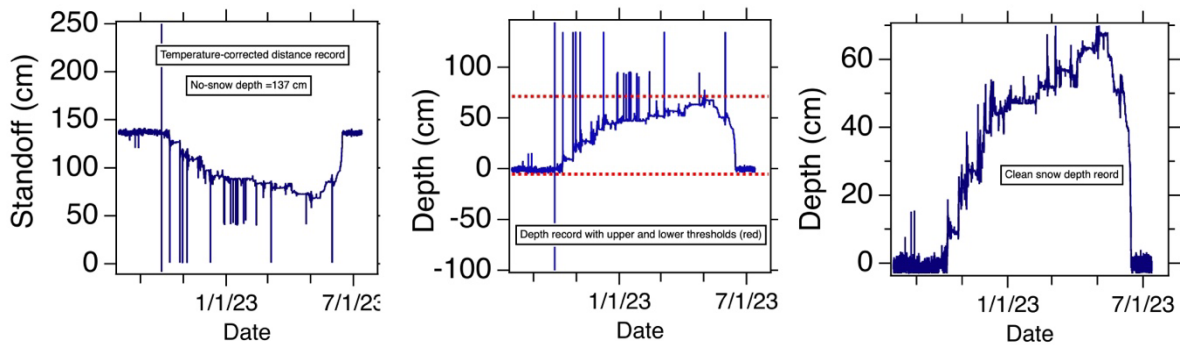


**Figure 5.** Converting sonic sounder raw values to a clean snow depth record. Panel 1: Distance to the snow with many spurious artifacts. Panel 2: Snow depth computed using Equation [1] and a no-snow depth; upper and lower thresholds for spurious data are indicated (red dashed lines). Panel 3: Spurious data removed; *NaNs* filled – a fairly clean depth record (no smoothing applied here).

Figure 6 shows a six-year depth record from the nine sounders at C1. The most salient feature is that in each winter, differences in depth between adjacent sensors range from 19 to 29 cm across the array, despite the total distance spanned between all sensors being less than 15 m. These local depth differences are driven by the site's micro-topography (more below), the prevailing wind, and the amount of drifting snow.

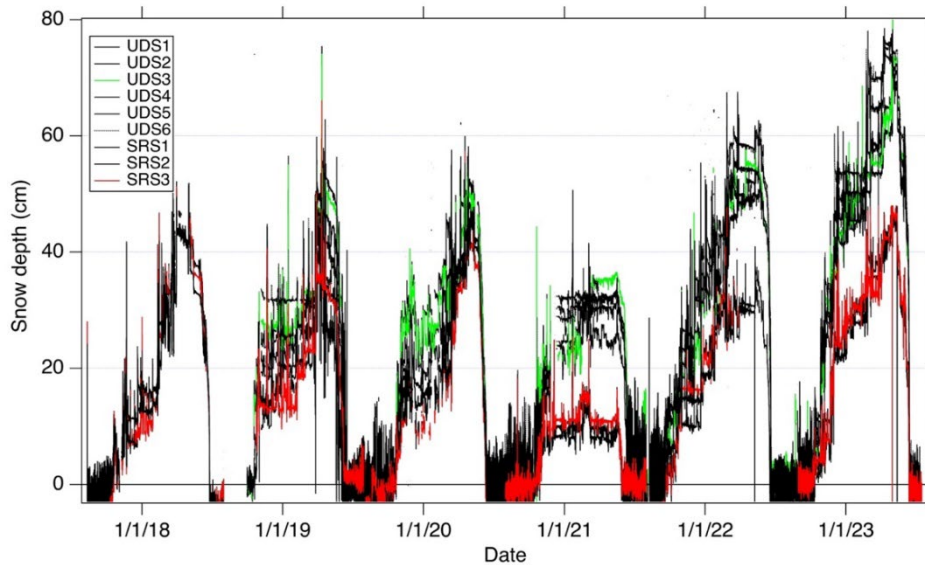


**Figure 6.** Snow depth from the nine sonic sounders at C1, 2018 to 2023. Green: Typical UDS. Red: Typical SRS. The difference is due to local tundra micro-topography, with the UDS over a trough and the SRS over a polygon top.

A second salient feature is that the mean snow depth at the site varies quite narrowly from year to year. Compared to alpine and maritime snow covers, the snow is always shallow. A “deep” year at C1 has 45 to 78 cm of depth locally, while a “shallow” year might report only 10 to 30 cm.

Third, the record is noisy (spikey) and does not always rise monotonically through the winter. Some of the spikes are artifacts that arise when there is blowing snow, confounding the sonic signal, but much of the noise is real because at C1 and E12, snow is both deposited and eroded multiple times, giving rise to frequent ups and downs in the record. Finally, though a little hard to discern in the condensed record shown in Figure 6, changes in snow depth are highly synchronous in timing from one sensor to another within an array, even if the change in depth is of opposite sign for two sounders. This synchronicity indicates the dominance of the wind in controlling the depth. This synchronicity extends between arrays as well, with E12 and C1 depths basically responding (depth up or down) at the same time, reflecting that over the 5.4 km separating the two arrays, wind events are synchronous.

We want to reinforce a critical point: that snow depth near C1 (and across much of the North Slope of Alaska) is extremely heterogeneous (cf. Sturm and Benson 2004). Figure 7A shows a 200-m depth profile (depth every meter) taken adjacent to the sonic sounder array at C1. While the average depth of the profile is consistent with the 2019 depths shown in Figure 6, the spatial depth range is 0 to 93.9 cm, with a CV (coefficient of variation) of 0.38. Figure 7B is an even longer snow depth profile (>1,000 m) taken adjacent to the E12 site showing a similar amount of spatial variation in depth (see Sturm and Holmgren 2018 for measurement protocol). Basically, the tundra snow at NSA exhibits considerable depth heterogeneity.

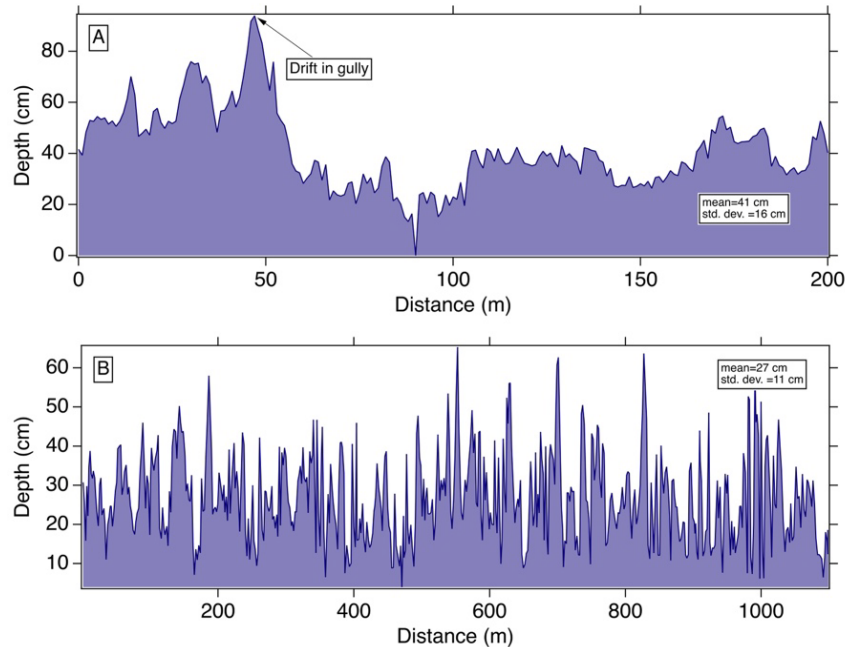


**Figure 7.** Panel A: A depth transect measured adjacent to the C1 sonic sounder array on May 16, 2019, showing the extreme depth heterogeneity at the site. Panel B: A similar but longer transect adjacent to the E12 array.

Two more detailed aspects of the sonic snow depth records have interpretive value with respect to the snow cover. First, the deposition of new fluffy snow (deposited in the absence of wind) can be inferred from characteristic settlement curves (Figure 8A). New snow is often more than 80% air and gravitational forces quickly lead to the snow settling and expelling that air. These curves, which can be readily fit using an exponential curve, are easily recognizable (Kojima 1967, Sturm and Holmgren 1998). However, at C1 and E12, snowfall without wind is relatively rare (Redilla et al. 2019), so finding such curves in the data record is infrequent. Second, wind transport of snow produces snow dunes that travel downwind, though at speeds considerably slower than the wind itself (0 to 15 meters/hour: Kochanski et al. 2019). Just as in sand deserts, wind acting on unconsolidated particles (ice in our case rather than quartz grains) produces a wide range of surface features ranging from ripple marks to barchans (crescent-shaped dunes) to wind waves (long dunes perpendicular to the wind) (Cornish 1902, Doumani 1966, Filhol and Sturm 2019). Since seasonal snow dunes have less than a year to grow (compared to centuries for sand dunes), they are smaller: usually no more than 50 cm high and less than 20 m in length. As a snow dune passes slowly beneath a sonic sounder, the snow depth goes up, then it goes down (Figure 8B), the time interval dependent on wind speed and dune size.

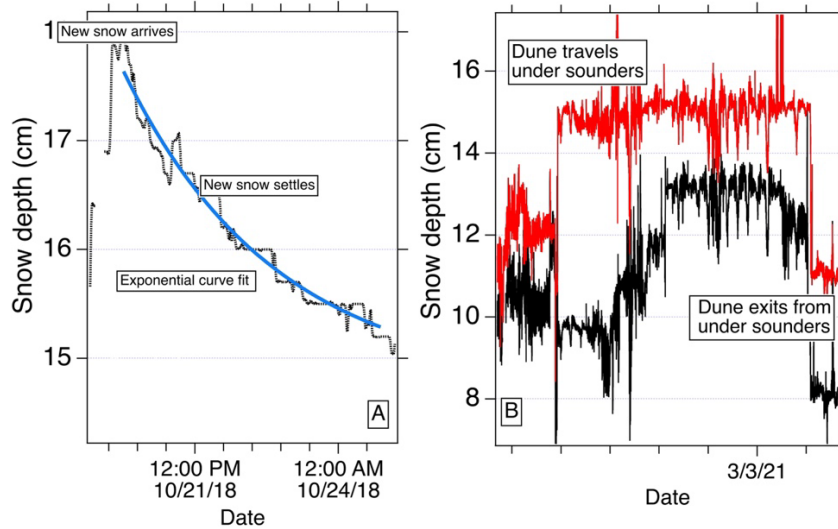


**Figure 8.** Panel A: A depth sounder record following the deposition of fluffy new snow. Panel B: The signal for a 4-cm-high dune migrating under two sounders (SRS#1 and SRS#3, C1). It arrives at slightly different times but exits about the same time from both sounders.

## 2.1 The Impact of Micro- and Meso-Topography on Snow Depth

Tundra is composed of tussocks and hummocks with relief that can range from 10 to 30 cm over distances of a few meters; at slightly larger scales (tens of meters), polygons and ice wedges create relief that can exceed 75 cm (Washburn 1956). Wind-drifting of snow interacts with this micro- and meso-topography to create depth variations of equal magnitude and wavelength and complex, seemingly contradictory behavior. Here, using examples, we show how the micro- and meso-topography at C1 affected the local snow depth records.

**Example 1:** Between October 26 and 29, 2022, about 0.7 cm of water equivalent (at a density of  $0.1 \text{ g/cm}^3$  this would convert to about 7 cm of new snow) was measured by the C1 LPM. As seen in Figure 9, this event had the opposite effect on the three upwind SRSs than it did on the six downwind Judd sounders. The former showed little change in depth, while the latter increased in depth by as much as 15 cm.

At the beginning of this event, despite a strong easterly wind, there was almost no snow to move, so the depths remained constant. Late on October 26, the wind subsided, and it started to snow. On the morning of October 27, after it had been snowing for a while, the wind picked up again, this time reaching speeds well above transport level (around 6 m/s). During this period, a 15-cm difference between sounders appeared in just a few hours (red versus green lines in Figure 9). Importantly, during these wind events, the upwind sounders initially recorded a slight increase in depth before decreasing, indicating there was an initial deposition of snow when the wind was insufficient to move it. This was followed by consistent scour, with the wind depositing the scoured snow into the downwind polygon troughs.

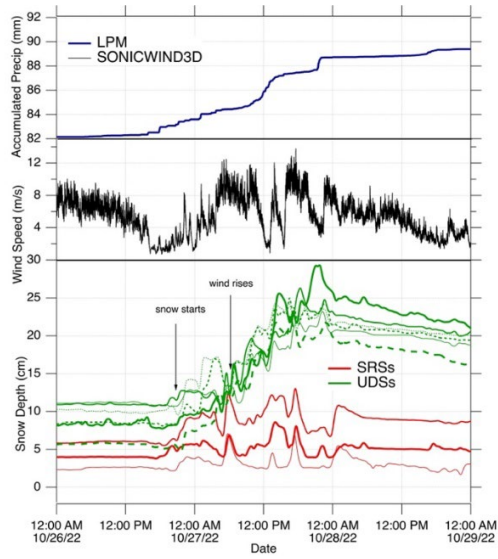


**Figure 9.** A snow event from the 2022-2023 winter illustrating local scour and fill within the sounder array. Top panel: accumulated precipitation (from the LPM). Middle panel: wind speed (from the sonic anemometer). Bottom panel: snow depth from the C1 array of sonic sounders. RED: SRSs on upwind polygon top; GREEN: downwind UDSs located above ice wedge trough.

A detailed topographic map of the array (Figure 10) explains the divergent behavior in snow depth. The three upwind sounders (which just happened to be SR50s [SRSs]) measure snow atop a high-centered polygon, while all the Judds (UDSs) measure snow depth in ice wedge troughs.

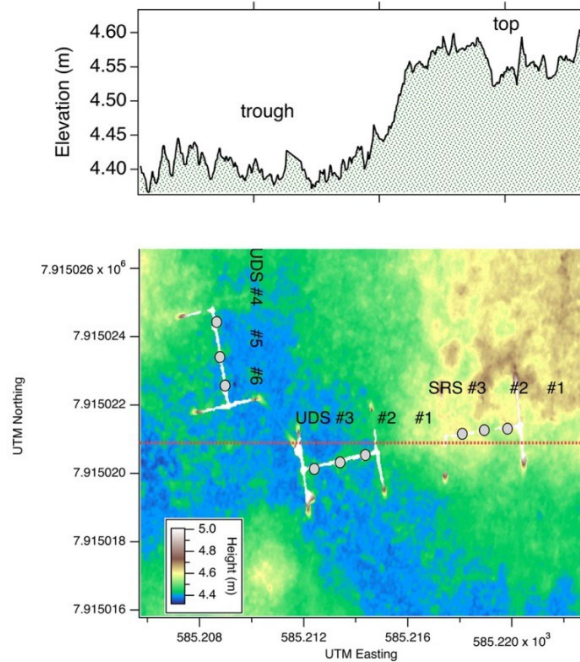


**Figure 10.** (Top) Elevation cross-section along red dashed line in the bottom panel with vertical exaggeration. (Bottom) Elevation map of the C1 swing sets. Blue areas are ice wedge troughs.

**Example 2:** The micro-topographic effect shown in Example 1 produced virtually the same divergent depth behavior again in the 2024 winter (Figure 11), with scour on the polygon top, and deposition in the adjacent ice wedge troughs.

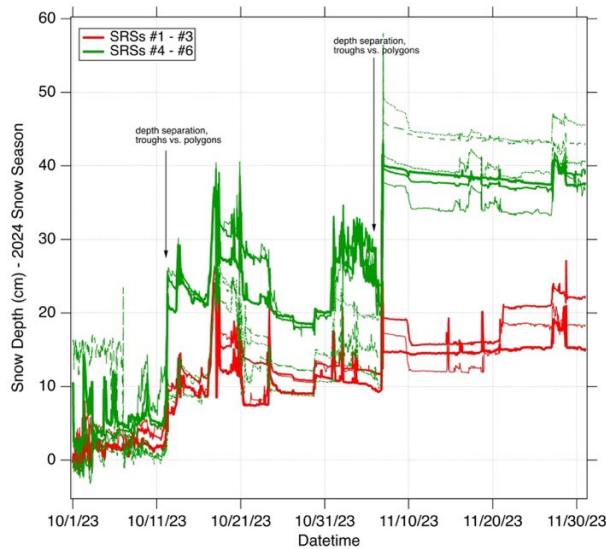


**Figure 11.** The winter of 2023-2024 produced the same divergent behavior in depth across the sounder array because the divergence is driven by the fixed micro-topography of the tundra. By 2024, the Judd sounders had been replaced by new SRSs. SRS #4 to #9, which replaced the Judds, were located over the ice wedge troughs (green traces) and indicated an increase in snow depth that was more than 20 cm greater than on the adjacent polygon top (red traces).

## 2.2 Data Quality Variable

The SRS datastream includes a data quality variable generated internally by the Campbell SR50s (Campbell Scientific 2016). The quality numbers have no units of measurement and range from 0 to 600 (Table 1).

**Table 1.** SRS data quality ranges.

Quality Number Range	Quality Range Description
0	Not able to read distance
152–210	Good measurement quality
210–300	Reduced echo signal strength
300–600	High measurement uncertainty

Reasons given for why quality values might fall outside the “Good Measurement Quality” range (152-210) are:

- Sensor is not perpendicular to the target surface
- Target is small and reflects little sound

- Target surface is rough or uneven
- Target surface is a poor reflector of sound (e.g., like extremely low-density snow).

In our analyses, we found that using the “Good Measurement Quality” range to parse the data produced mixed results. It led to the removal of too many valid data points while also failing to eliminate some clearly erroneous data. This dual negative effect can be observed in both Figures 12 and 13. For example, during the winter of 2021-2022, as the snow depth increased in a stair-step manner, nearly 40% of all the measurements fell into the uncertain quality category. While removing these uncertain data left a cleaner, more easily interpreted depth record (Figure 12 bottom), Figure 13 illustrates how the same filtering process left some spurious data spikes while also discarding valid depth data.

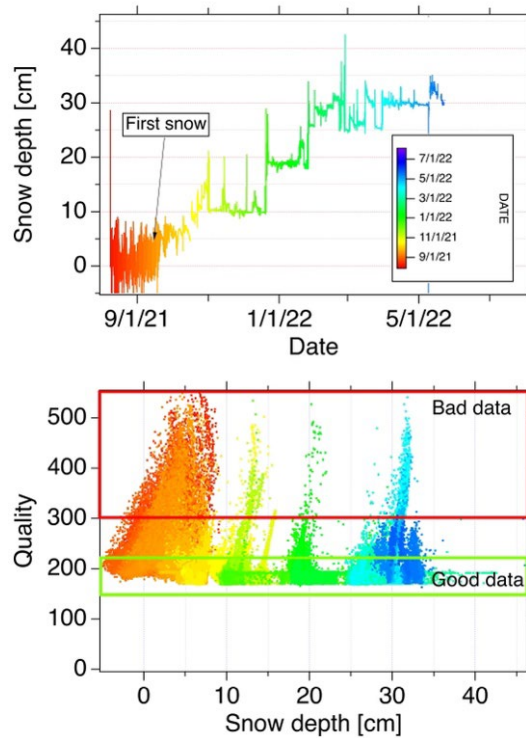


**Figure 12.** Top: Snow depth for the winter of 2021-2022, color-coded by measurement date. Bottom: Quality measurements for the same data using the same color-coding. Note the preponderance of bad data (red-orange) prior to first snowfall, but also that three times during the winter, considerable bad data are indicted (green to blue).

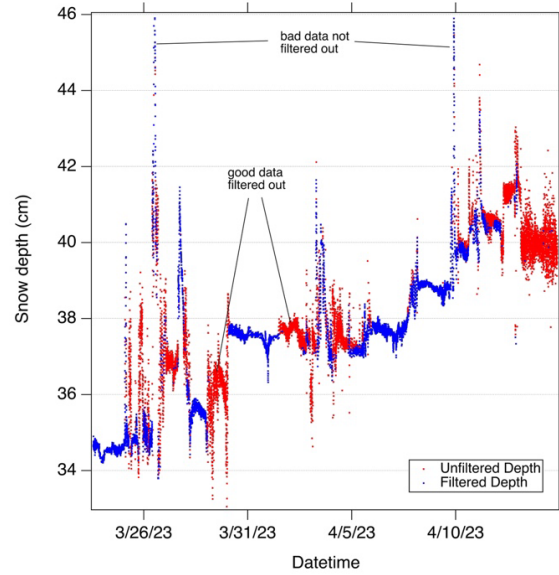


**Figure 13.** An example of unfiltered depth data (red dots) overlain by only data with quality values between 152 and 210 (blue dots). As the gaps in the overlay show, considerable valid data was removed by the filtering, while some bad data also remained.

We investigated whether high wind and/or blowing snow might have produced the poorer-quality values (>210) but found no evidence of causality (Figures 14 top and bottom). The examples plotted in the figures are from the winter of 2023, but similar results were found at E12 for the same winter and in other winters for C1.

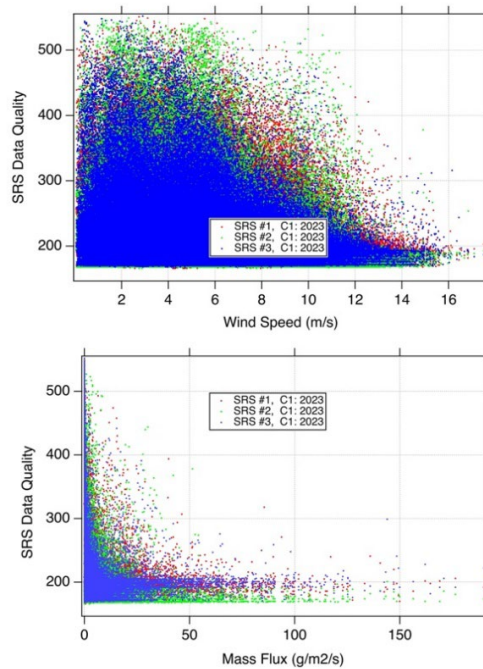


**Figure 14.** Data quality values as a function of wind speed (top) and drift flux (bottom). We would expect to see an increase in poorer-quality values (>210) with increasing wind and drift, but do not.

Based on these analyses, we recommend that the Campbell Scientific-derived quality values not be used as a filter due to the number of useful measurements removed from the data set, though we continue to archive these values and ensure they are available.

### 3.0 Wind

We operate a Thies-Clima heated 3D sonic anemometer mounted 2 m above the ground (<https://www.thiesclima.com/en/Products/Wind-measuring-technology-Ultrasonic-Anemometer/>: Figure 15). It is called the SONICWIND3D or U3D. The instrument reports the  $u$ ,  $v$ , and  $w$  (vertical) wind vectors every 10 seconds. The  $w$ -vector is positive upward; the  $u$ - and  $v$ -vectors are the easterly and northerly components of the horizontal wind, respectively. No processing is done on the  $u$ -,  $v$ -, and  $w$ -data before they are ingested into the ARM Data Center, but for the analysis here, we compute from the  $u$ - $v$  vector sum to produce the horizontal wind speed and its azimuth (See Appendix B). With respect to the accuracy of those speeds, we have compared the reported SONICWIND3D horizontal wind speeds to the wind speeds measured by other anemometers at ARM and found that they correlate to the U3D with an  $r^2 = 0.871$  and agree in magnitude. Our experience has been that the SONICWIND3D is an extremely reliable device, and we note that even during riming events, it continues to produce accurate wind data.



**Figure 15.** Thies-Clima three-dimensional sonic anemometer (SONICWIND3D). In the background is the double Alter shield surrounding the LPM.

The wind blows hard and nearly continuously during the winter at C1 (Figure 16). For example, over the winter of 2022-2023, it averaged 4.6 m/s. At E12, it averaged 4.8 m/s. For comparison, in “windy” Fargo, North Dakota, the wind averages about 5 m/s (NDSU 2024). With respect to the snow conditions at both C1 and E12, however, the more relevant statistic is the percentage of the time the wind exceeds 6 m/s. Research has shown (Tabler 1994, Li and Pomeroy 1997, Sturm and Stuefer 2013) that, on average, winds of 6 m/s will erode and entrain snow. Such winds were exceeded almost 30% of the year at C1

(2,425 hours in 2022-2023). Results from E12 were similar at 29% of the time. This high frequency of >6 m/s wind is more than sufficient to transport vast quantities of snow. The exceedance percentage (percent in excess of) drops to 3% for winds of 10 m/s, and to 0.03% for 15 m/s, which is a good thing for the people living in Utqiagvik.

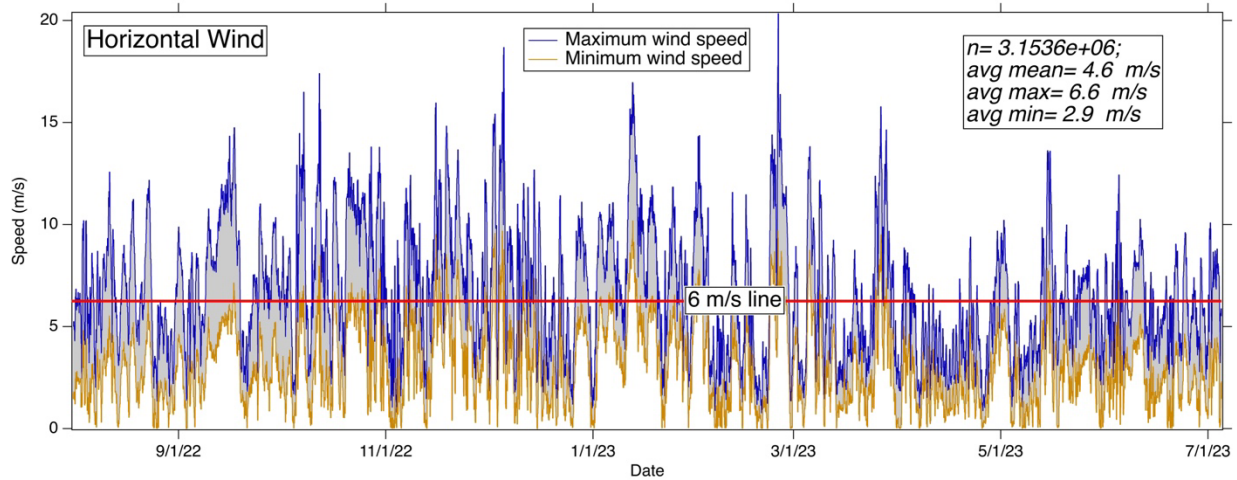


**Figure 16.** Minimum and maximum wind speeds for 2022-2023 at C1. On average, 6 m/s (red line) is sufficient to entrain and transport snow.

The prevailing wind direction at C1 and Utqiagvik in general is from the northeast and east (Figure 17). The wind rose for E12 is similar to C1.

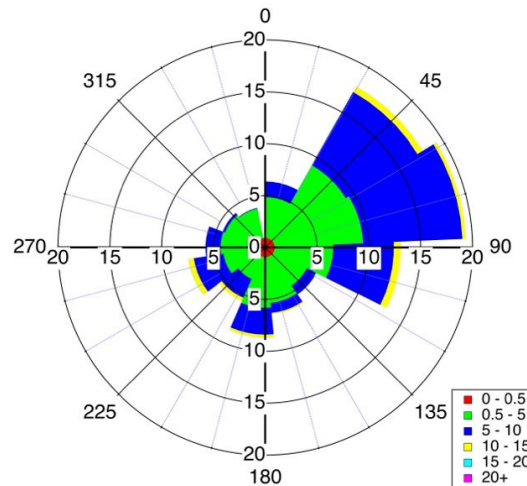


**Figure 17.** Wind rose for C1 from the winter of 2022-2023. Note that the predominant winds come from the NE and E.

The vertical wind at C1 oscillates between -0.6 and +0.6 m/s. This is an important value because it represents the ability of the wind to loft snow particles from the ground. There is weak positive relationship between the horizontal wind and the vertical wind ( $r^2=0.1$ ; Figure 18) and there is some indication that the strength of the vertical wind also depends on the direction of the wind itself. This is a

reasonable supposition because the wind fetch is obstructed to the north and northeast of the location of the SONICWIND3D anemometer by distant buildings, but not from other directions.

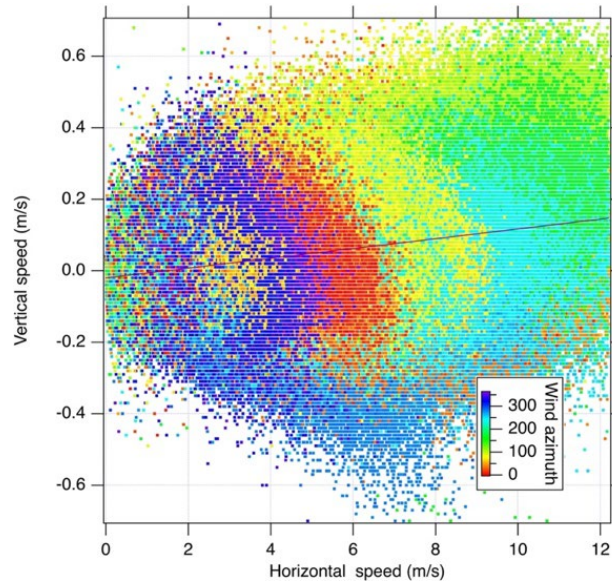


**Figure 18.** Vertical wind speed ( $w$ ) as a function of the horizontal wind speed. The colors indicate the wind azimuth. There is a cluster of data around horizontal speed 6 m/s for winds from the north (red dots). There is a slight increase in positive vertical wind speed (updrafts) with increasing horizontal wind speed (black regression line).

## 4.0 Blowing Snow

We operate a pair of FlowCapt blowing snow sensors at C1 and a second pair at E12 (we call these the SPMFs) (<https://www.isaw-products.com/flowcapt-fc4/>). They are hollow metal tubes, each one meter long, stacked one above the other, facing into the wind. A microphone and hard-wired signal analyzer use the frequency of snow particles impinging on the tubes to compute the horizontal flux of snow while the wind speed is computed from the vibrational resonance of the tube in the wind stream. The blowing snow fluxes are computed for a lower and upper flux gate with units of  $\text{g}/\text{m}^2/\text{s}$  (see Figure 19). An extensive analysis and explanation of the results from the FlowCpts (SPMF) can be found in Trouvilliez et al. (2015).

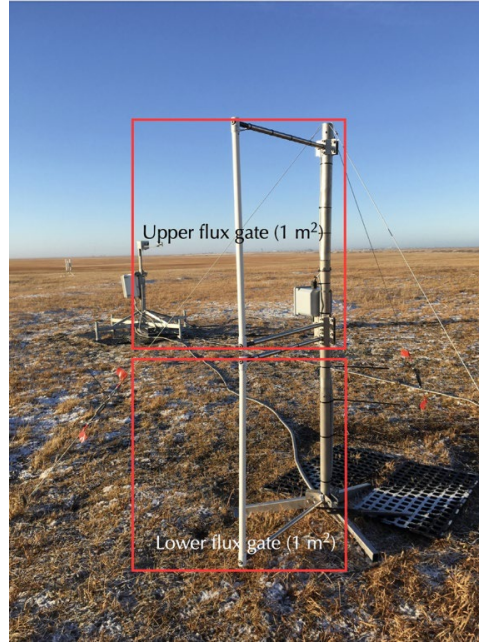


**Figure 19.** Upper and lower FlowCapt units (SPMFs), seen here facing into the prevailing E and NE winds. The theoretical flux gate areas over which the measurements are made are shown in red. The unshielded LPM at C1 is the background.

The SPMF is a factory-calibrated device, with the calibration taking an empirical form:

$$q = A \times S^B \text{ (millivolts)} \quad [2]$$

where  $q$  represents the calibrated snow mass flux ( $\text{g}/\text{m}^2/\text{s}$ ) calculated using the manufacturer's values for  $A$ ,  $S$ , and  $B$ .  $S$  denotes the amplified and filtered signal from particle impacts (received at the data logger in mV). The constant  $A$  varies for each SPMF instrument and is determined through a factory testing procedure with a controlled flux of polyvinyl chloride (PVC) particles, while  $B$  is fixed at 2. Only  $q$  is recorded and archived.

The SPMF wind speed is measured as the wind blows around the tube and causes vortex shedding. The frequency at which vortex shedding takes place for an infinitely long cylinder is related to the Strouhal number ( $S_t$ ) by the following equation:

$$S_t = \frac{fD}{V} \quad [3]$$

where  $f$  is the frequency of the vortex shedding [ $\text{s}^{-1}$ ],  $D$  is the tube diameter, and  $V$  is the fluid (air) flow velocity.  $S_t$  is approximately 0.22 for a wide range of Reynolds Numbers, and  $D$  is 0.032 m, so [3] reduces to a simple formula for wind speed as a function of vibration frequency:

$$V = f \cdot D/S_t = f \cdot (0.032/0.22) = 0.145 \cdot f \quad [4]$$

## 4.1 Mechanisms of Snow Transport

To understand the output from the SPMFs, one needs to understand how the wind transports snow. It is well established that it travels in three modes (Tabler 1994) (Figure 20):

1. **Creep:** grains rolling and sliding along the snow surface.
2. **Saltation:** grains bounding along the snow surface and impacting and ejecting other grains (usually limited to the lowest 30 cm above the snow surface).
3. **Suspension:** small particles that settle slowly are lofted tens to hundreds of meters.

Modes 1 and 2 generally account for most of the wind transport of snow until the wind exceeds 20 m/s (Table 2); hence, we would expect much lower values from the upper SPMF tube than the lower one, and indeed, that is what we observe. With the SPMFs spanning 0 to 2 m height and wind speeds at NSA C1 generally less than 10 m/s, in theory, the setup samples 90% of the total wind-blown flux of snow.

Table 2 (Tabler 1994) can be used to better understand the SPMF flux measurements. Assume a wind speed of 10 m/s. The table indicates that between 0 and 0.1 m height, 82.2% of the total blowing flux will be found. From 0.1 to 1.0 meters, an additional 8.7% more flux will be found, for a total of 90.9%. But if the wind rises to 20 m/s, the bulk of the drifting snow moves much higher above the ground (only 25.1% now being found below 0.1 m, while 40% additional snow is between 0.1 and 1.0 m). We can conclude from the table that the ARM SPMFs, spanning 0 to 2 meters (in one-meter segments), sample somewhere between 94% and 79% of the drift flux at C1 and E12, with the low bias rising during those infrequent periods when the wind exceeds 20 m/s. Notably, the total flux rises more than an order of magnitude as the wind rises from 10 to 20 m/s.



**Figure 20.** Three modes of wind transport of snow.

**Table 2.** (Tabler 1994): Vertical fraction of snow transport as a function of wind speed.\*

Height Z (m)	Wind speed (m/s)				
	10	15	20	25	30
0.1	0.822	0.487	0.251	0.126	0.056
0.2	0.853	0.579	0.365	0.239	0.160
0.3	0.868	0.628	0.431	0.312	0.233
0.4	0.878	0.661	0.480	0.366	0.290
0.5	0.885	0.687	0.519	0.411	0.338
1.0	0.909	0.768	0.645	0.563	0.505
1.5	0.925	0.818	0.725	0.662	0.616
2.0	0.938	0.857	0.786	0.737	0.701
2.5	0.950	0.888	0.834	0.797	0.770
3.0	0.961	0.915	0.876	0.849	0.828
3.5	0.971	0.940	0.912	0.893	0.879
4.0	0.981	0.961	0.944	0.933	0.924
4.5	0.991	0.981	0.973	0.968	0.964
5.0	1.000	1.000	1.000	1.000	1.000
	(32.3)	(114.9)	(375.0)	(902.0)	(1711.8)

m/s = 0.447 (miles/h)

\*Tabulated values are the fraction of total transport at height Z divided by the total transport in the bottom 5-m of the air. The total snow transport amount [g/m/s] is shown at the bottom in parentheses.

The total measured blowing snow flux, as measured by the SPMFs (adding the top and bottom values together), ranges over five orders of magnitude and is not easy to visualize, so it is worthwhile to consider what these flux values mean. In Table 3, we have computed for a range of fluxes (0.1 to 1,000 g/m<sup>2</sup>/s) the size of a snowball that could be made from the flux through a gate after one full day of snow transport.

**Table 3.** Snowball sizes due to 24 hours of drift flux.

Flux [g/m <sup>2</sup> /s]	Flux [cc H <sub>2</sub> O/day]	*Snow volume [cm <sup>3</sup> ]	Snowball radius [cm]
0.1	8640	14400	15.1
1	86400	144000	32.5
10	864000	1440000	70.1
100	8640000	14400000	150.9
1000	86400000	144000000	325.2

\*Computed assuming a snow density of 0.6 g/cm<sup>3</sup>.

## 4.2 SPMF Wind Speed

We do not generally use the wind values reported from the SPMFs. The devices report minimum, mean, and maximum one-minute values. Comparing the mean values from the lower and upper SPMFs (Figure 21) to the more accurate sonic anemometer, the bottom SPMF under-reports the wind speed by a significant amount, which is not surprising because it measures the wind about 1.5 m lower than standard height. The upper SPMF comes closer to the correct value but still under-reports. Note also that the

SPMFs are relatively insensitive to wind speeds less than 3 m/s, showing zero readings up to winds at that speed. At high wind speeds ( $>10$  m/s), the SPMFs over-report the speed by significant and unpredictable amounts. If the SPMF wind speed is the only data available, we recommend only using the values from the upper unit, using the maximum rather than the mean, and discarding values more than 10 m/s.

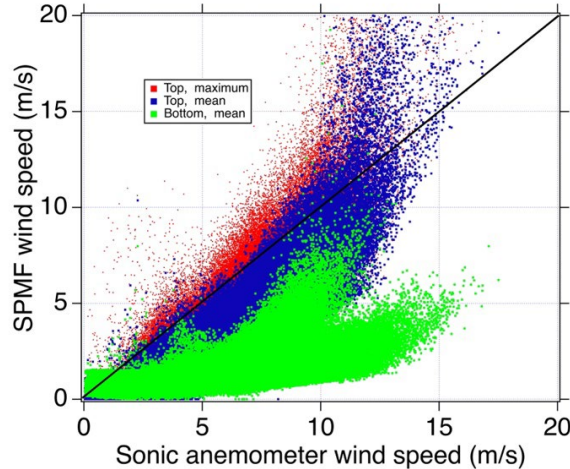


**Figure 21.** SPMF versus sonic anemometer (U3D) wind speeds. Green: Bottom SPMF mean wind values. Blue: Top SPMF mean wind values. Red: Top SPMF wind maximum values. The black line is the 1:1 line. SPMF wind speeds are unreliable above 10 m/s.

### 4.3 SPMF Flux Measurements

The flux characteristics recorded by the SPMF output are displayed in Figure 22 for the SPMFs at C1. The reporting interval is every 10 seconds; however, we have created one-minute averages of the mean fluxes for this analysis. These averages indicate that there is often a tenfold difference between the upper and lower flux values, attributed to the dominant transport modes of creep and saltation. The fluxes exhibit a striking correlation with wind speed once the wind surpasses 6 m/s (Figure 23), rising and falling in tandem with the fluctuations in wind speed (Figure 22).

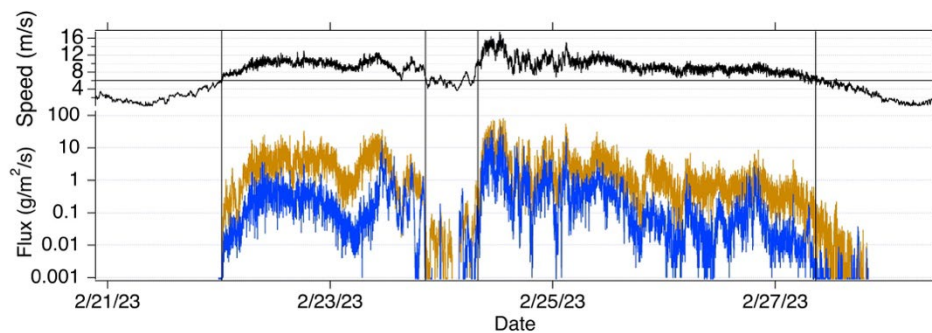


**Figure 22.** An example of SPMF flux data: upper (blue) and lower (gold) SPMF mean values. The wind speed (from the U3D) is shown in the top panel in black: the fluxes exhibit remarkable fidelity with the wind speed, as expected.

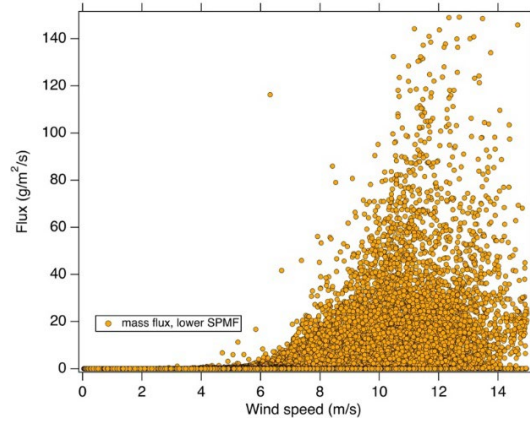


**Figure 23.** SPMF lower sensor snow flux as a function of U3D wind speed. Until a threshold of 6 m/s wind speed is achieved, there is little measurable flux. An extensive literature discussing this threshold is summarized in Sturm and Stuefer (2013). In principle, the threshold should vary with deposited snow hardness, but at C1 ( $n=525,600$ ), there is little evidence for much snow transport below 6 m/s.

The SPMF is an empirically calibrated device. Checking reported values in the field, particularly in the Arctic, is nearly impossible because the instrument records little flux until the onset of a blizzard, when making measurements becomes extremely difficult. We have to look elsewhere for the device's accuracy. Trouvilliez et al. (2015), following a detailed comparison study in the Alps, concluded that the SPMF is a reliable blowing snow event detector but that it underestimates the actual mass flux. The low values are particularly prevalent during combined snowing and blowing events and when the flux exceeds 20 g/m<sup>2</sup>/s.

Our local observations support this assessment. If we compare the SPMF flux as a function of wind speed at C1 to the drift flux observed at many other snowy sites (data from Sturm and Stuefer 2013), we find it is, in general, as much as a factor of 10 lower (Figure 24).

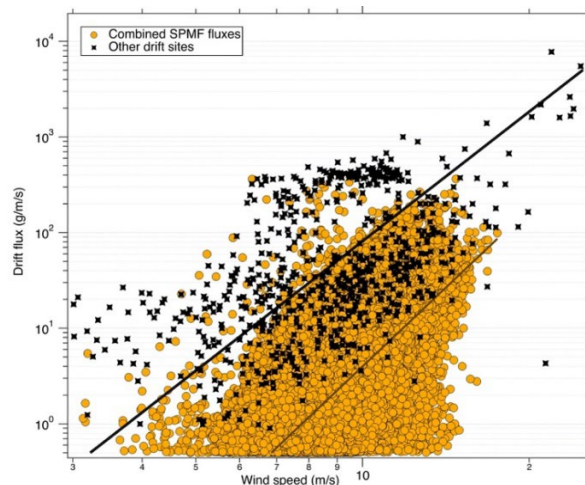


**Figure 24.** The drift flux at C1 as measured by the SPMFs (gold circles) compared to the drift flux observed at other comparable snowy locations (black diamonds) (from Sturm and Stuefer 2013). Note the SPMF flux is consistently lower by more than a factor of 10.

We can make a second comparison using a large drift captured by the snow fence protecting Cake Eater Road about 5 km west of C1. Between 2007 and 2011, we measured the volume of the drift over a dozen times. While it varied from one year to the next, the volume near the end of winter averaged about  $140 \text{ m}^3$  of snow/lineal meter of fence. It has been shown for an efficient snow fence that the deposited volume is equal to the total winter wind-blown flux if the capacity of the fence is not exceeded, which is rare at Cake Eater (Tabler 1994). Integrating the combined bottom and top SPMF fluxes for the 2022-2023 snow year, we get a total flux of about  $44 \text{ m}^3$  of snow/lineal meter, or about one-third of what accumulates adjacent to the fence, consistent with low bias of the SPMFs shown in Figure 24. Some of this discrepancy accrues because the fetch at C1 is blocked to the NE and E by roads, ditches, and buildings that winnow out snow that otherwise would have impinged on the sensors, while the Cake Eater fence has essentially an unlimited fetch of snow (Figure 25). However, the main reason for the SPMFs' under-reporting of the flux is likely the same issues discussed by Trouvilliez et al. (2015).

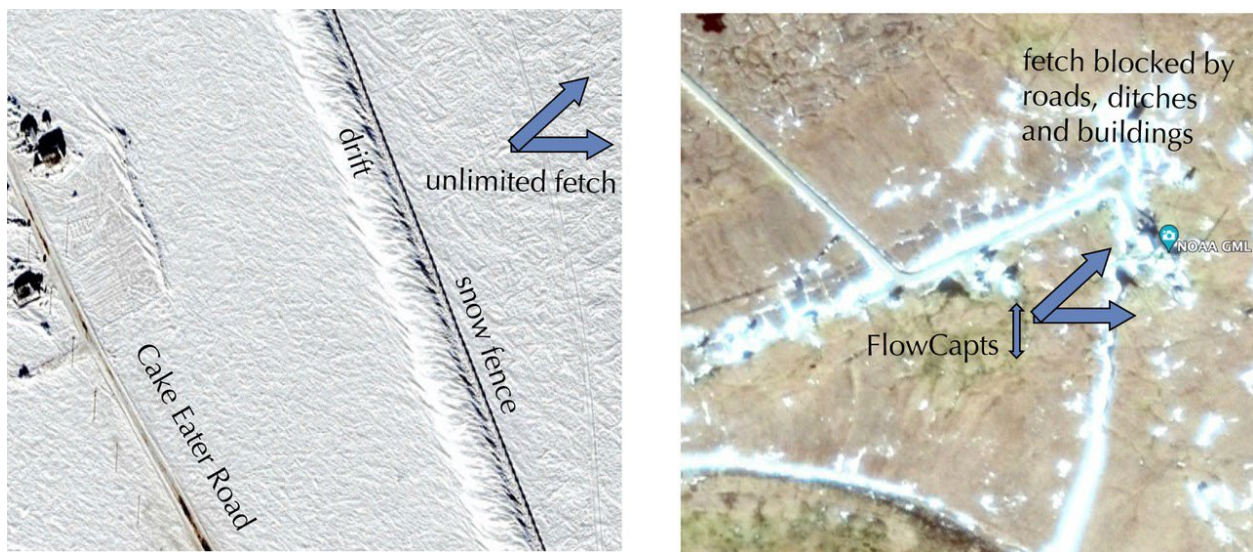


**Figure 25.** Comparison of the Cake Eater snow fence and the C1 SPMFs. At C1, there are obstructions 150 m upwind (prevailing direction) that are likely reducing the flux at the sensors, in addition to the tendency for the SPMFs to underestimate the flux in general.

## 5.0 Totalizing Precipitation Gauge (WBGEONOR or Geonor)

NOAA's Global Monitoring Laboratory (GML) operates a Geonor vibrating wire totalizing precipitation gauge (Bakkehoi et al. 1985, Duchon 2008) surrounded by a DFIR wind fence. A recent inspection suggests the fence is in poor shape and that a large drift develops around and downwind of the gauge; the quality of the precipitation measurements is unknown. The Geonor we operate at E12 is relatively new (2023), and we do not have sufficient experience at this point to make a useful assessment of the device. However, in Figure 26, we have compared the E12 Geonor accumulation (values from all three vibrating wires) to the total accumulation measured by the C1 LPM: over much of the record the agreement is satisfactory, though there are strong deviations early and late in the winter that we are still working to explain. Riming and clotting of snow at the orifice of the Geonor gauge can lead to under-measurement of the precipitation (if the rime does not fall into the weighed bucket) and might account for these deviations, as might data handling operations.

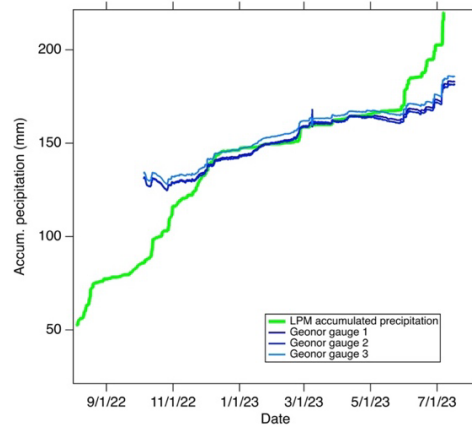


**Figure 26.** Comparison of the E12 Geonor totalizing precipitation gauge with the C1 accumulated precipitation from the LPM.

## 6.0 Falling Snow and Rain

At NSA C1, we operate one wind-shielded (C1) and one unshielded (E10) Thies-Clima laser precipitation monitor (LPM) (Figure 27: See Thies-Clima 2008:

<https://www.thiesclima.com/en/Products/Precipitation-measuring-technology/>). At E12, we operate a single shielded LPM, devices also called present weather sensors (PWS) or disdrometers (Löffler-Mang and Joss 2000). A horizontal laser plane is projected across a gap such that any particle or hydrometeor falling through the plane casts a shadow on a photo-diode array on the receptor side of the instrument. This allows the instrument to measure the particle fall speed and its “size,” typically the widest horizontal dimension. Internal proprietary algorithms use that information and the known characteristics of falling hydrometeors to classify the particle as rain or snow, and if snow, to assign a density from which precipitation intensity (mm H<sub>2</sub>O/hour) can be computed. The wind shields around the LPMs are Belfort Double Alter shields (see Figure 15 in the background and Kochendorfer et al. 2017).



**Figure 27.** The C1 unshielded LPM. (E10 operated at the C1 site).

The instrument bins falling particles into 22 sizes and 20 fall speed classes (Table 4), reporting 440 values every minute, along with many other weather and quality parameters. Other useful variables included in the one-minute telegram are precipitation intensity (solid, liquid, and total: mm/hour), 5-minute average precipitation intensity (mm/hour), and the total number of particles falling per minute/square meter. Synoptic weather codes are also reported.

**Table 4.** LPM disdrometer size and fall speed classes.

Particle diameter class			Particle speed class		
Class	Diameter [mm]	Class width [mm]	Class	Speed [m/s]	Class width [m/s]
1	≥ 0.125	0.125	1	≥ 0.000	0.200
2	≥ 0.250	0.125	2	≥ 0.200	0.200
3	≥ 0.375	0.125	3	≥ 0.400	0.200
4	≥ 0.500	0.250	4	≥ 0.600	0.200
5	≥ 0.750	0.250	5	≥ 0.800	0.200
6	≥ 1.000	0.250	6	≥ 1.000	0.400
7	≥ 1.250	0.250	7	≥ 1.400	0.400
8	≥ 1.500	0.250	8	≥ 1.800	0.400
9	≥ 1.750	0.250	9	≥ 2.200	0.400
10	≥ 2.000	0.500	10	≥ 2.600	0.400
11	≥ 2.500	0.500	11	≥ 3.000	0.400
12	≥ 3.000	0.500	12	≥ 3.400	0.800
13	≥ 3.500	0.500	13	≥ 4.200	0.800
14	≥ 4.000	0.500	14	≥ 5.000	0.800
15	≥ 4.500	0.500	15	≥ 5.800	0.800
16	≥ 5.000	0.500	16	≥ 6.600	0.800
17	≥ 5.500	0.500	17	≥ 7.400	0.800
18	≥ 6.000	0.500	18	≥ 8.200	0.800
19	≥ 6.500	0.500	19	≥ 9.000	1.000
20	≥ 7.000	0.500	20	≥ 10.000	10.000
21	≥ 7.500	0.500			
22	≥ 8.000	∞			

Rainfall precipitation rates from the LPMs are more accurate than snowfall rates. At terminal velocity, falling raindrops take on a predictable shape (e.g., the shape of the top of a hamburger bun; Figure 28) that can be mathematically described, and from which droplet volume and mass can be computed (McDonald 1954, Beard and Chuang 1987, Gorgucci et al. 2006). The fall speed of these droplets follows the well-known Gunn-Kinzer terminal velocity curve (Gunn and Kinzer 1949, Bosio et al. 2023: Figure 29), and we have been informed by Thies-Clima that liquid droplets falling at speeds that deviate from the curve are automatically discarded from the count. The LPMs assume any hydrometeor falling at air temperatures greater than +9°C is liquid and that any hydrometeor falling at air temperatures below -4°C is solid. From -4°C to +9°C, we believe the size and nature of the hydrometeor is determined by the fall speed (e.g., slower falling hydrometeors are solid or mixed phase because their mass-to-surface-area ratios are lower).

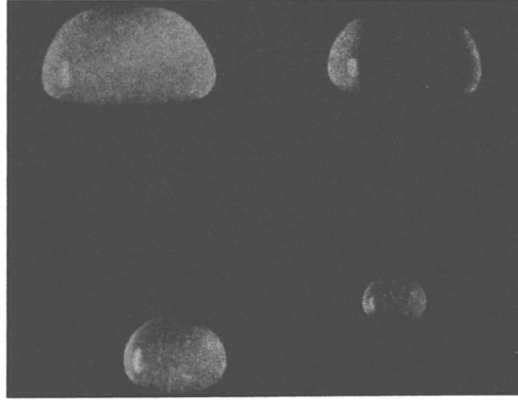
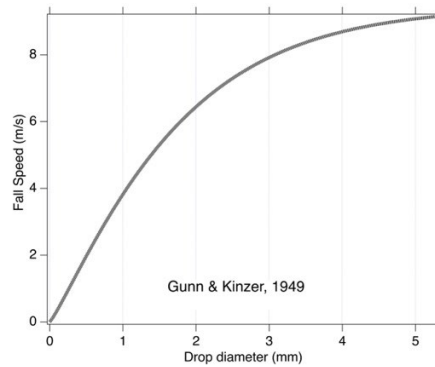


FIG. 1. Large water drops falling at terminal velocity (see Magono, 1954). Equivalent spherical diameters and measured fall velocities as follows: upper left, 6.5 mm and 8.9 m/sec; upper right, 6.0 mm and 8.8 m/sec; lower left, 4.8 mm and 8.3 m/sec; lower right, 2.8 mm and 6.8 m/sec.

**Figure 28.** Raindrops at terminal velocity (from McDonald 1954).



**Figure 29.** The Gunn-Kinzer curve for raindrops falling at terminal velocity.

With respect to snow precipitation rates, the complex shapes and variable densities of falling snow particles create problems. Battaglia et al. (2010) discussed some of the inherent limitations of disdrometers when measuring solid precipitation:

- They typically report the largest horizontal dimension of a particle as it falls through the laser plane, which may not be a good measure of the size of a particle with a complex shape (e.g., a stellar dendrite).
- Particles falling on the margin of the laser may be assigned an erroneous size.
- Particles falling through the laser plane obliquely will register apparent fall speeds that are lower than true fall speeds; wind-accelerated particles can move faster than terminal velocity for a given size and shape.
- It is assumed only one particle is passing through the laser at any one time.

Some method of going from particle size (ostensibly the largest horizontal dimension,  $D$ ) to the particle mass ( $m$ ) is required, where:

$$m = \rho_P V \quad [5]$$

with  $\rho_P$  the individual particle density and  $V$  the particle volume. Often, an empirical power-law relationship is used to relate  $D$  to  $m$ , by-passing the need to make assumptions about particle shape for volume, etc.

$$m = \alpha D^\beta \quad [6],$$

where  $\alpha$  and  $\beta$  empirical parameters.

Extensive literature relates types of snow crystals and crystal aggregates to particle densities, the degree of riming, and fall speed. Mitchell et al. (1990) provide values for  $\alpha$  and  $\beta$  as a function of the snow crystal type for 19 different crystals. Vázquez-Martín et al. (2021a, 2021b) update these relationships and provide empirical equations relating maximum dimension to fall speed and mass. As Figure 30 shows, there is no unique relationship between particle mass ( $m$ ) and maximum dimension ( $D$ ). The algorithm used to convert snow crystal size and fall speed to a mass precipitation rate in the Thies-Clima LPM is proprietary, and efforts to learn this algorithm have not been successful. We think that perhaps the conversion from maximum dimension ( $D$ ) to water equivalent uses a fall speed-mass conversion with average (for all crystal types)  $\alpha$  and  $\beta$  parameters. Regardless, the instrument, lacking any way to obtain information on crystal type and degree of riming, must use a conversion that is at best a rough estimate and should be treated as such. Thus, LPM intensity values for solid precipitation (mm/hr) should be used with caution.

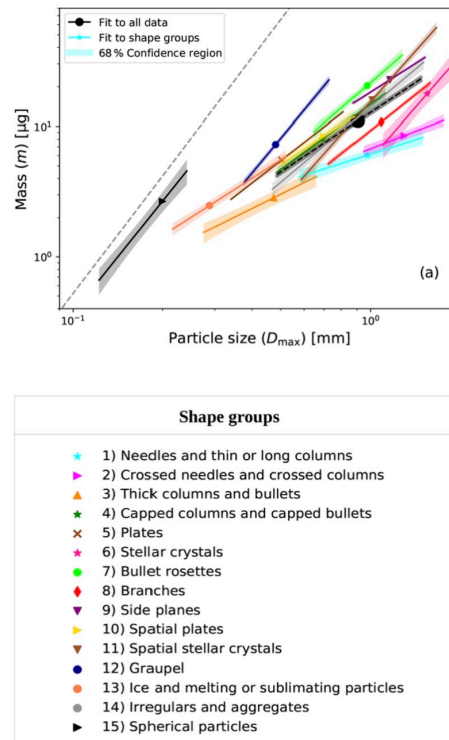


**Figure 30.** Mass as a function of particle diameter and crystal type from Vázquez-Martín et al. (2021a).

Despite these limitations, Fehlmann et al. (2020), in a recent paper, assessed the efficacy of the Thies-Clima LPM for measuring snow precipitation with encouraging results. Comparing the LPM in low-wind conditions to a totalizing precipitation gauge and a 2D particle photographic system, they found

that: a) the LPM separated the precipitation into rain, snow, and mixed-phase precipitation correctly 95% of the time, though significantly, b) correction factors have to be applied to the particle counts to adjust for over-counting in the smallest size bins. Their correction factors are listed in Table 5. They also provide a functional relationship between  $D$  and  $\rho_P$  (Figure 31) that is very useful. We note, however, that the arctic environment of C1 and E12 is quite different from that at the Swiss test site used by Fehlmann et al. (2020), and therefore, their findings need to be extrapolated with caution.

**Table 5.** Correction factors for LPM size bins (from Fehlmann et al. 2020).

Class (no.)	Range (mm)	Rain correction factor	Snow correction factor
1	0.125–0.25	0.92	0.43
2	0.25–0.375	0.83	0.55
3	0.375–0.5	0.92	0.68
4	0.5–0.75	1.08	0.78
5	0.75–1	1.57	1.26
6	1–1.25	1.40	1.25
7	1.25–1.5	1.43	1.21
8	1.5–1.75	1.38	1.20
9	1.75–2	1.35	1.19
10	2–2.5	1.29	1.20
11	2.5–3	1.18	1.21
12	3–3.5	1.10	1.18
13	3.5–4	0.92	1.12
14	4–4.5	0.88	1.11
15	4.5–5	0.81	1.08
16	5–5.5	0.63	1.04
17	5.5–6	0.34	1.04
18	6–6.5	0.70	1.02
19	6.5–7	0.29	1.02
20	7–7.5	0.17	1.02
21	7.5–8	0.17	1.01
22	> 8	0.19	1.06

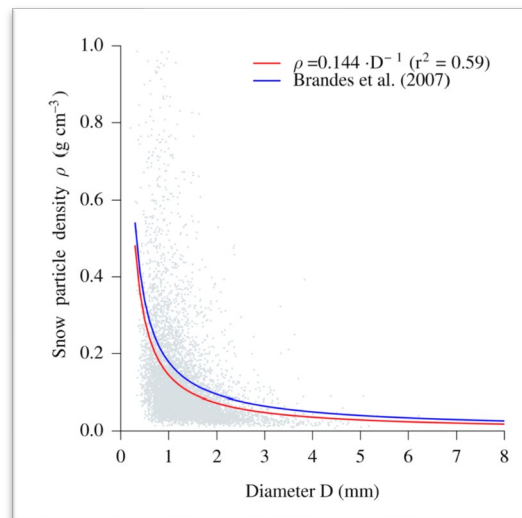


**Figure 31.** From Fehlmann et al. (2020), a functional relationship between maximum horizontal diameter ( $D$ ) and particle density for snow ( $\rho$ ).

## 6.1 Examples of LPM Events

Reporting over 400 values per minute, LPM results can be confusing. To best understand the uses and limitations of the LPM data, real examples serve best. The first example (December 30, 2022, to January 4, 2023) is typical of many winter events, and it shows the effect of wind and blowing snow on the LPM measurements. It was  $-12^{\circ}\text{C}$  during this entire event, while the wind varied from 0 to 8 m/s (Figure 32). On December 28, there was a high particle count, with the E10 count noticeably higher than the C1 count. Note that E10 and C1 LPMs are 16 m apart, with C1 shielded and E10 unshielded. The December 28 high-count rate did not produce a significant intensity value (mm H<sub>2</sub>O per hour) at either instrument because the count was driven by a large number of very small particles. As the wind began to drop (December 30), the intensity of precipitation increased. During that period, as long as the wind remained above 6 m/s, the E10 intensity was notably higher than the C1 intensity, but when the wind dropped to near zero, the two measurements converged. As the wind rose again, E10 again began to exceed C1 in counts and intensity.

We think the difference in counts between the adjacent LPMs is explained by blowing snow particles, which are often tiny due to wind pulverization. Apparently, these ice fragments were lofted and more readily blew into the unshielded E10 LPM than the shielded C1 LPM, though we cannot exclude that some of the count and intensity at C1 was also due to snow blown up from the tundra and into the counting laser plane. Confirming this hypothesis, Figure 33 shows that during the low-wind segments of this event, the E10 count approached a 1:1 ratio with the C1 count, but that during the high-wind periods, the E10 count ran almost twice as high as C1.

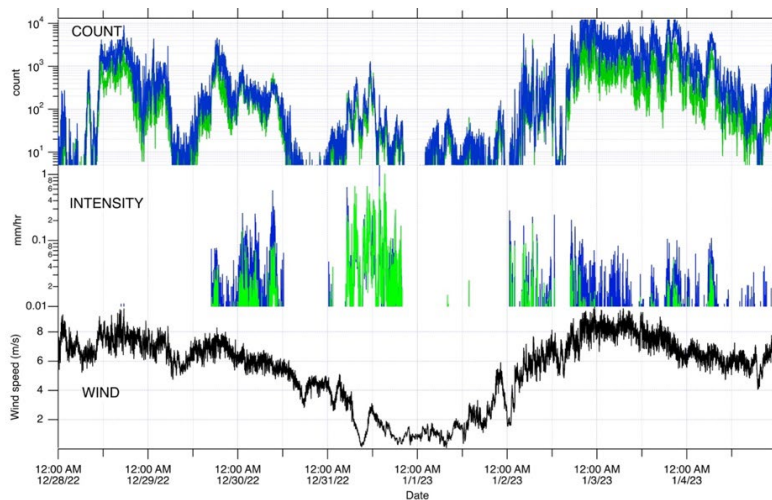


**Figure 32.** The LPM event of January 1, 2023. Note that at higher wind speeds, the shielded C1 (green) trace is visible beneath the E10 trace (blue). This suggests that LPMs report similar data in low winds, but the unshielded LPM detects significantly more particles at higher wind speeds than the shielded instrument. This relative behavior provides strong evidence that blown snow is counted by the unshielded gauge when the wind exceeds 6 m/s.

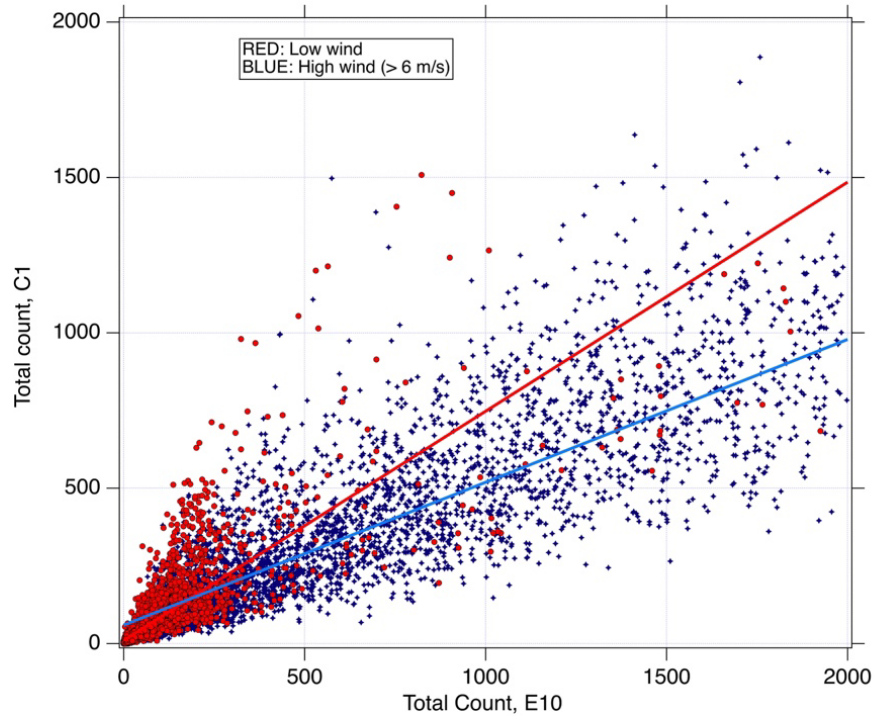


**Figure 33.** C1 LPM total counts versus E10 total counts for the January 1 event. Red=low wind (< 6 m/s); Blue= high wind ( $\geq 6$  m/s). At low winds the data come closer to a 1:1 line than during high winds, suggesting that the unshielded E10 instrument counts wind-driven particles that do not contaminate the C1 LPM count.

A second example is from August 5, 2022, and is a mixed-phase (rain and snow) event. Table 6 illustrates how the instrument produces hydrometeor counts by size and fall speed for each one-minute scan. During the event, the air temperature was  $+8^{\circ}\text{C}$ , just short of the LPM cutoff for allowing snow measurements, and the wind was low (< 4 m/s). At the shielded C1 LPM, there were about equal amounts of rain and snow, but at the unshielded E10 LPM, there was only rain (Figure 34). Despite this difference in precipitation type, the total particle counts (number of particles/minute/ $\text{m}^2$ ) for the two instruments were similar (Figure 35): a total of 44,106 particles were counted by the C1 LPM versus 36,062 by the E10. Contour plots of these totals, however, separated into diameter and fall speed classes, show that more large particles (e.g., raindrops versus snow crystals) fell at E10 than at C1, and these larger particles fell faster overall than the mixed snow and rain at C1, as we would expect (Figure 36). The example confirms that the shielded and unshielded LPMs report similar results in low-wind conditions and illustrates several ways the LPM data can be analyzed.

**Table 6.** August 5, 2022 event LPM number counts (C1 top; E10 bottom).

C1_August5_2022_Event																						C1_Count
FallSpeed	FallSpeed	FallSpeed	FallSpeed	FallSpeed	FallSpeed	FallSpeed	FallSpeed	FallSpeed	FallSpeed	FallSpeed	FallSpeed	FallSpeed	FallSpeed	FallSpeed	FallSpeed	FallSpeed	FallSpeed	FallSpeed	FallSpeed	FallSpeed	FallSpeed	ByDia
Bin1	Bin2	Bin3	Bin4	Bin5	Bin6	Bin7	Bin8	Bin9	Bin10	Bin11	Bin12	Bin13	Bin14	Bin15	Bin16	Bin17	Bin18	Bin19	Bin20	Bin21	Bin22	
DiameterBin1	32	334	899	1441	1852	3389	2426	1395	803	451	265	257	104	41	34	12	6	0	0	0	0	13741
DiameterBin2	4	34	142	358	669	2149	2345	1669	874	418	271	336	154	82	48	23	16	16	3	9	9	9620
DiameterBin3	1	19	53	117	203	770	1288	1472	746	245	105	129	38	11	4	7	0	0	0	0	0	5208
DiameterBin4	0	5	18	45	72	258	696	1739	2465	1499	559	310	26	5	3	1	0	0	0	0	0	7701
DiameterBin5	0	0	4	12	9	23	70	142	340	756	951	865	90	6	1	0	0	0	0	0	0	3269
DiameterBin6	0	1	1	2	8	14	46	119	135	150	323	878	239	8	0	1	0	0	0	0	0	1925
DiameterBin7	0	0	0	3	2	9	13	55	75	104	100	305	266	83	3	1	0	0	0	0	0	1019
DiameterBin8	0	0	1	2	0	4	7	31	54	51	85	111	143	95	24	1	0	0	0	0	0	609
DiameterBin9	0	0	0	1	0	3	7	14	22	38	47	85	41	66	54	3	0	0	0	0	0	381
DiameterBin10	0	0	0	0	1	3	2	9	14	40	42	73	60	32	68	40	3	0	0	0	0	387
DiameterBin11	0	0	0	0	0	1	0	2	0	3	15	42	26	19	14	21	14	3	0	0	0	160
DiameterBin12	0	0	0	0	0	0	0	0	0	0	0	8	9	8	2	6	7	5	1	0	0	46
DiameterBin13	0	0	0	0	0	0	0	0	0	0	0	1	4	0	5	1	2	7	2	0	0	22
DiameterBin14	0	0	0	0	0	0	0	0	0	1	0	0	1	0	3	0	0	3	0	0	0	8
DiameterBin15	0	0	0	0	0	0	0	1	0	0	0	1	0	0	0	1	0	0	0	0	0	4
DiameterBin16	0	0	1	0	0	0	0	2	0	0	0	0	0	0	1	0	0	0	0	0	0	4
DiameterBin17	0	0	0	0	0	0	0	0	0	0	0	1	0	0	0	0	0	0	0	0	0	1
DiameterBin18	0	0	0	0	0	0	0	0	1	0	0	0	0	0	0	0	0	0	0	0	0	1
DiameterBin19	0	0	0	0	0	0	0	0	0	0	0	0	0	0	0	0	0	0	0	0	0	0
DiameterBin20	0	0	0	0	0	0	0	0	0	0	0	0	0	0	0	0	0	0	0	0	0	0
DiameterBin21	0	0	0	0	0	0	0	0	0	0	0	0	0	0	0	0	0	0	0	0	0	0
DiameterBin22	0	0	0	0	0	0	0	0	0	0	0	0	0	0	0	0	0	0	0	0	0	0
TOTAL	37	393	1119	1981	2816	6623	6900	6650	5529	3756	2763	3402	1201	456	264	118	48	34	6	10	10	
E10_August5_2022_Event																						E10_Count
DiameterBin1	11	130	478	629	746	1342	995	695	484	303	219	258	104	43	22	7	2	0	0	0	0	6468
DiameterBin2	3	88	229	424	628	1833	1626	861	509	324	278	339	199	115	48	18	8	5	0	1	1	7536
DiameterBin3	5	37	140	213	226	698	1587	1268	535	243	156	219	90	36	7	5	2	2	0	0	0	5469
DiameterBin4	1	47	109	132	131	225	432	1706	2413	1616	806	511	95	14	3	2	0	0	0	1	1	8244
DiameterBin5	0	7	14	14	14	15	17	10	52	320	1003	1683	290	18	1	0	0	0	0	0	0	3458
DiameterBin6	0	4	7	8	7	6	8	6	4	6	51	1040	873	103	2	0	0	0	0	0	0	2125
DiameterBin7	0	1	0	4	4	5	4	2	6	3	7	84	567	397	37	0	0	0	0	0	0	1121
DiameterBin8	0	0	1	2	2	4	1	2	1	2	1	7	154	336	164	14	0	0	0	0	0	691
DiameterBin9	0	0	2	2	1	3	1	1	2	0	1	5	15	118	158	61	0	0	0	0	0	370
DiameterBin10	0	1	1	2	1	0	2	2	2	2	1	5	9	53	150	122	39	1	0	0	0	393
DiameterBin11	0	0	0	1	1	2	0	1	2	1	1	3	2	7	19	41	41	4	0	0	0	126
DiameterBin12	0	0	0	0	0	1	1	1	0	1	0	2	1	0	3	9	10	10	2	0	0	41
DiameterBin13	0	1	0	1	0	1	0	0	0	0	0	0	0	0	2	0	3	1	3	0	0	12
DiameterBin14	1	0	0	0	0	0	0	1	0	0	0	0	0	0	1	1	0	1	0	1	0	5
DiameterBin15	0	0	0	0	0	0	0	0	0	0	0	0	0	0	0	0	0	0	0	0	0	0
DiameterBin16	0	0	0	0	0	0	1	0	0	0	1	0	0	0	0	0	0	0	0	0	0	2
DiameterBin17	0	0	0	0	0	0	0	0	0	0	0	0	0	0	0	0	0	0	0	0	0	0
DiameterBin18	0	0	0	0	0	0	0	0	0	0	0	0	1	0	0	0	0	0	0	0	0	1
DiameterBin19	0	0	0	0	0	0	0	0	0	0	0	0	0	0	0	0	0	0	0	0	0	0
DiameterBin20	0	0	0	0	0	0	0	0	0	0	0	0	0	0	0	0	0	0	0	0	0	0
DiameterBin21	0	0	0	0	0	0	0	0	0	0	0	0	0	0	0	0	0	0	0	0	0	0
DiameterBin22	0	0	0	0	0	0	0	0	0	0	0	0	0	0	0	0	0	0	0	0	0	0
TOTAL	21	316	981	1432	1761	4135	4675	4556	4010	2821	2525	4156	2400	1240	616	280	106	23	6	2	2	

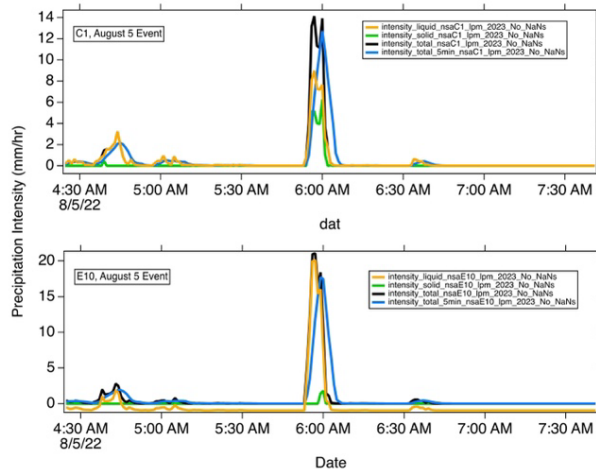


**Figure 34.** C1 (shielded) and E10 (unshielded) LPM intensity responses to the mixed-phase event on August 5, 2022, which was quite brief.

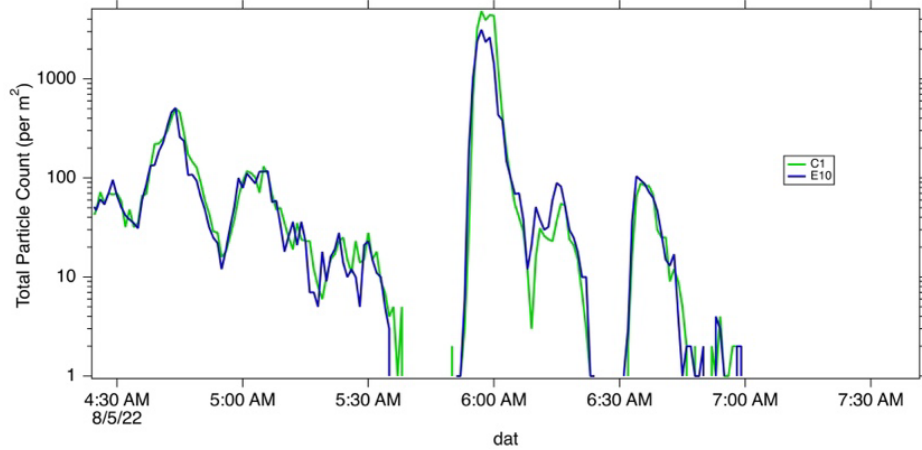


**Figure 35.** Particle counts, C1 and E10, during the August 5 event.

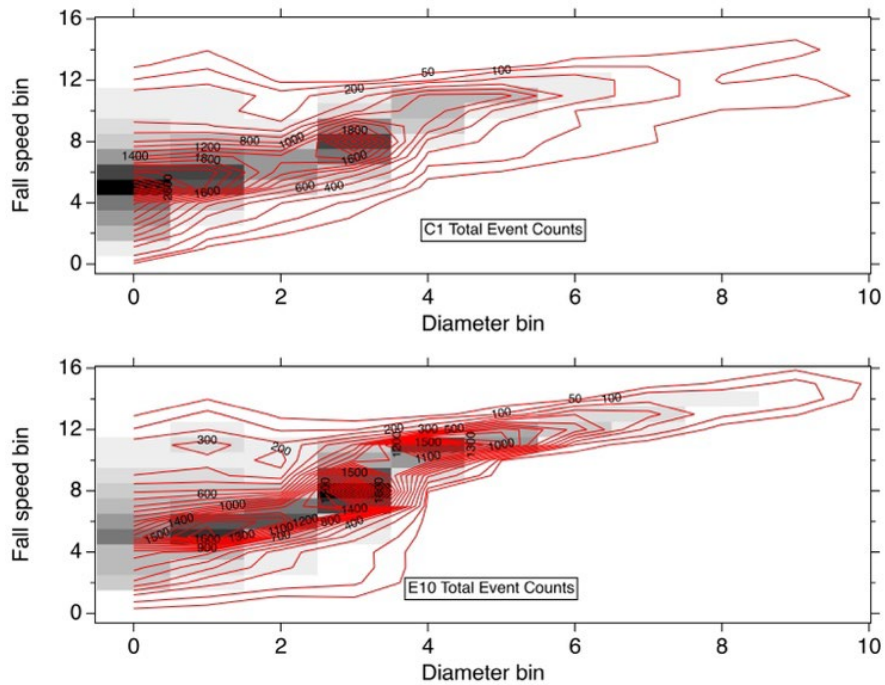


**Figure 36.** The distribution of particles by size and fall speed for the August 5 event (contours are of total counts) shows similar values.

The third and final example (February 25, 2023) is an event characterized by very high winds (>16 m/s), where it is possible that there was no precipitation at all, despite substantial recorded LPM counts and intensities. This was a cold event, meaning all the particles were solid hydrometeors. As shown in Figure 37, the increase in intensity during the event correlated with the rise in wind speed, and for the most part, C1 and E10 exhibited similar values.

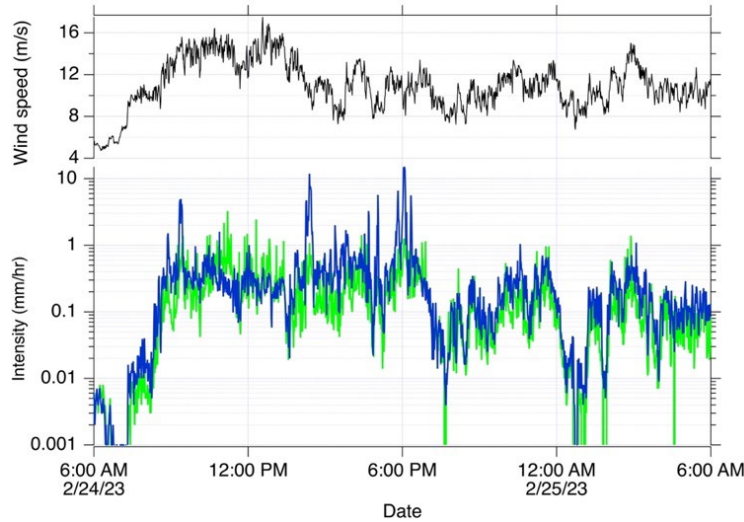


**Figure 37.** February 25 event: the intensity rises with the wind speed and is the same for C1 (green) and E10 (blue).

The distribution functions for E10 and C1 were nearly identical, with 95% of all particles coming in the first two diameter bins and 99% in the first three bins (Figure 38), consistent with the size of particles found in blowing snow under high winds. In the blizzard conditions that prevailed during this event, there would have been no way to check whether there was actual precipitation (video cameras were obscured, etc.), but we can examine what was happening to snow on the tundra during the event (Figure 39). On the ground, all sonic sounders showed erosion of the snow surface. Between 2 and 8 cm were removed by the wind during the event, more than an ample supply, if there was a mechanism to loft it to the height of the LPMs. Up- and down-drafts of the wind were averaging  $\pm 0.5$  m/s, suggesting that indeed there was enough turbulence to loft the eroding snow.

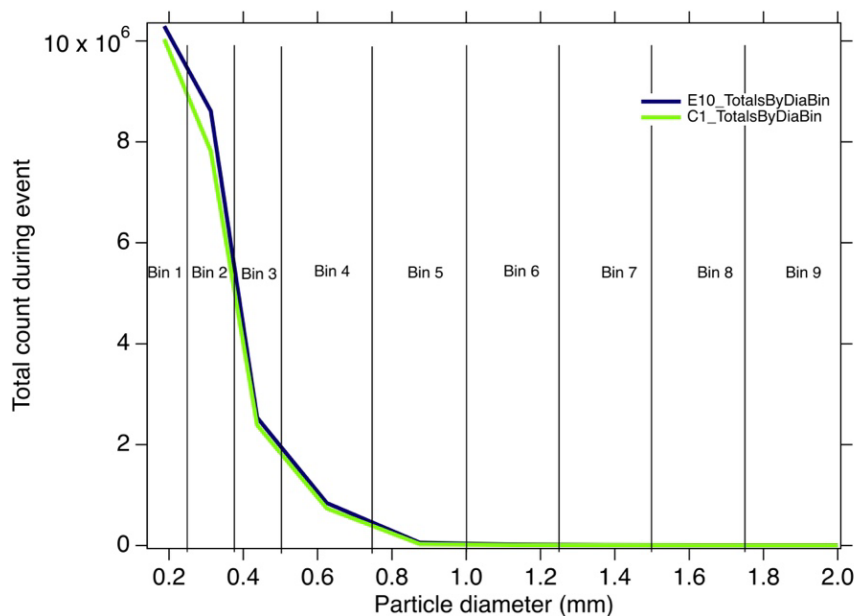


**Figure 38.** Particle distribution curves plotted by diameter and bin number. Note that C1 and E10 are nearly identical; 95% of all particles were in the first two bins.

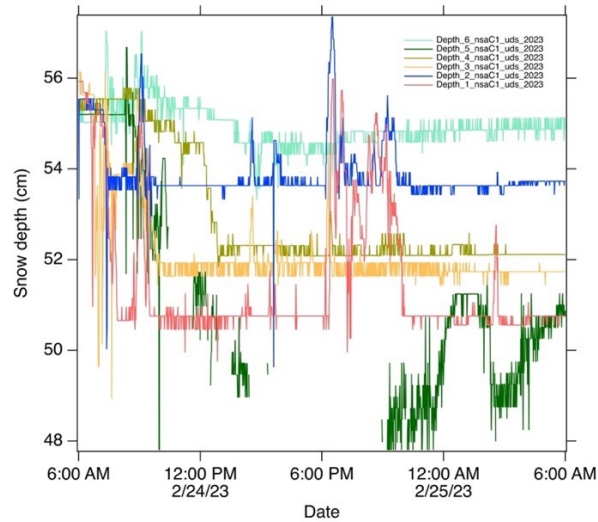


**Figure 39.** Snow erosion under the sonic sounders during the February 24-25, 2023, event.

In conclusion, LPMs are known to work reasonably well in snowy climates where wind is limited. However, at C1 and E12, where winter winds are relentless, it is probable that the apparent precipitation intensities may include snow swept up from the tundra. In the strongest winds, it is possible that nearly all recorded precipitation is tundra snow that has been lifted and counted as precipitation multiple times. Having one shielded LPM and one unshielded LPM presents the opportunity to differentiate the source of the LPM snow.

## 6.2 Particle Count Comparisons of C1 and E10 LPMs

Comparing the shielded (C1) and unshielded (E10) LPMs at NSA, the following observations can be made about particle counts (Figures 40 and 41):

1. E10 typically records a greater number of particles per minute than C1. This can be seen in Figure 40, where the points lie above the 1:1 line for most of the data.
2. The differences between the two LPMs are structured with wind speed. The highest counts typically are recorded during the highest wind speeds. One possible reason for this is that wind acceleration of particles could push more particles through the LPM gap per minute than when there is no wind acceleration. A second possible reason is that wind speeds higher than 6 m/s cause snow lofting from the tundra snow, which could increase the number of particles being counted.
3. At the lowest wind speeds, the counts tend to converge between C1 and E10, hitting the 1:1 line.
4. However, at the highest speeds ( $> 12$  m/s), the normal comparison reverses, and C1 exceeds E10 in the counts for reasons that are presently unclear.

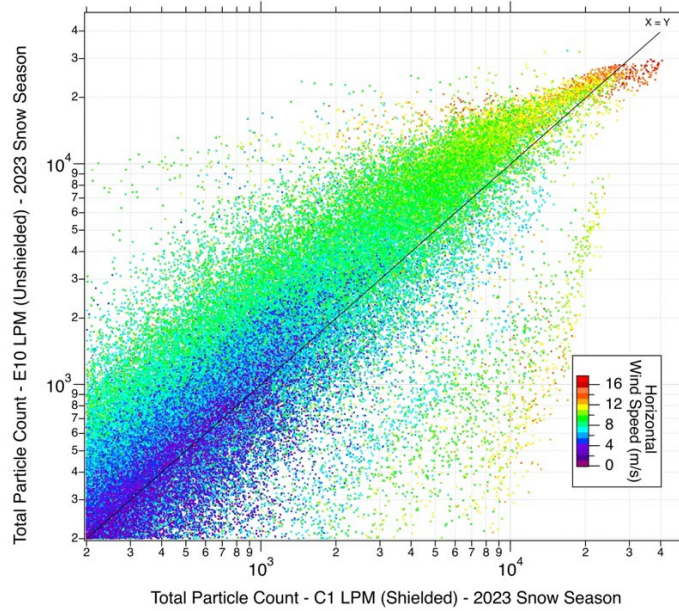


**Figure 40.** Comparison of the E10 and C1 LPM hydrometeor counts for the winter of 2023. Each dot represents a value from a one-minute record, color-coded by wind speed. Note that for all speeds except the highest (>12 m/s), E10 counts slightly more particles than C1; however, above 12 m/s, this trend reverses.

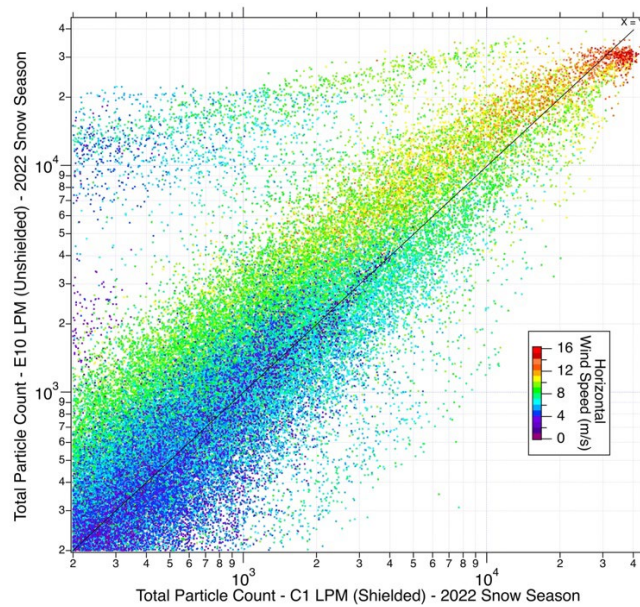


**Figure 41.** Same as above but for the 2022 winter.

### 6.3 Comparing C1 and E12

The rationale for installing E12 about 5.4 km south of C1 was that over a 30-year period, we had anecdotally noted that winter weather conditions at E12 were sometimes different than nearer the coast. Currently, we have only two years of data for comparison, but our observations suggest:

- There is distinctly more winter precipitation at C1 than at E12 (Figures 42 and 43), nearly 50 mm of water equivalent (over a winter total of about 150 mm) at C1.
- Wind speeds and directions are quite similar between the two sites (Figure 43) and synchronous when they shift and change.
- The drift flux as reported by the SPMFs may be more intense at C1 than E12 (Figure 44), though this finding is sensitive to small differences in placement height of the lower SPMF above the snow surface at the sites. We noted that the E12 sensor was slightly higher than the C1 in 2024.

While we expected differences between C1 and E12, the differences listed above, if confirmed with more data, are substantial over such a short distance, and suggest that the snow regime at C1 is affected by its proximity to the ocean, which is less than a kilometer away and is a good source of moisture.

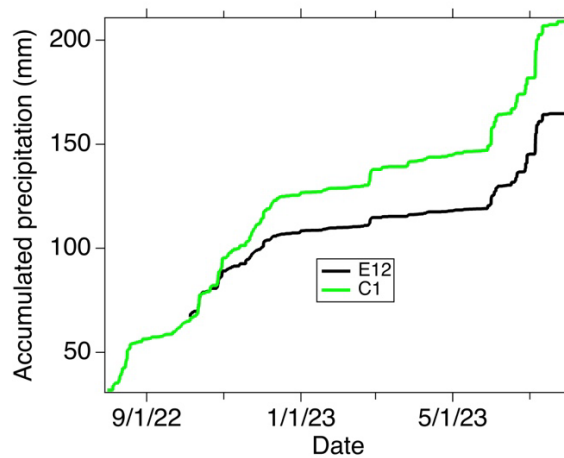


**Figure 42.** Accumulated winter precipitation for C1 (green) and E12 (black) showing significantly more precipitation at C1.

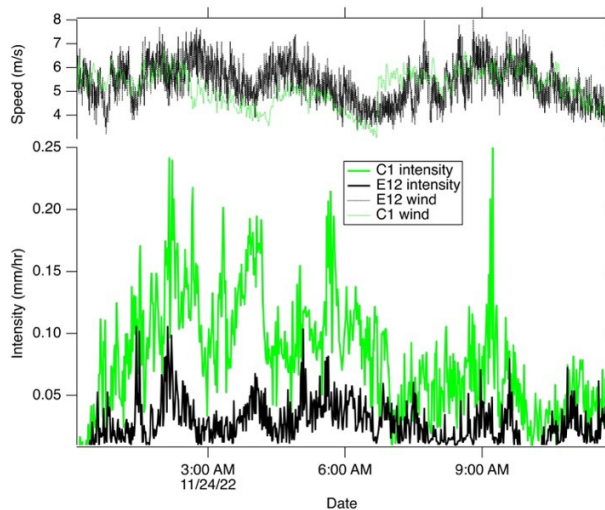


**Figure 43.** LPM intensities (bottom panel) and wind speeds (top) for C1 (green) and E12 (black).

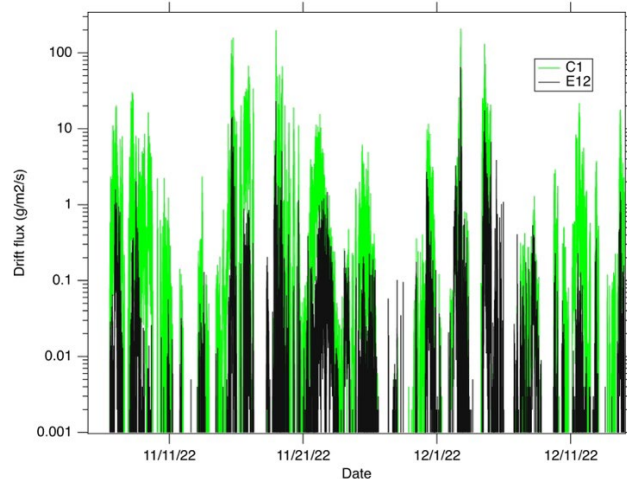


Figure 44. The drift flux from the SPMFs at C1 (green) and E12 (black).

## 7.0 Using Multi-Instrument Ensemble Data to Better Understand the Snow Cover Evolution

As the examples in the previous sections show, snow from the tundra can be lofted high enough to pass through the LPM laser plane, getting counted as precipitation, thereby rendering the precipitation measurements (intensity values) unreliable. While our current understanding suggests that under lofting conditions the reported precipitation exceeds the true precipitation, we cannot rule out that wind acceleration might also produce the opposite effect, with particles failing to pass through the LPM laser plane, or failing to enter the Geonor orifice in high winds. At the same time, snow depth can increase or decrease during the winter multiple times. Using all the instruments at C1 and E12 in concert, conditions in which the precipitation values are reliable (versus suspect) could potentially be identified automatically, as well as establishing when wind erosion versus deposition predominates. It should be possible to correct measured values through instrument-instrument comparisons. Toward that end, Table 7 lists the four possible snow conditions that can exist at C1 and E12.

Table 7. Wind, snowfall, and drift conditions at C1 and E12.

Condition	Snowfall	Drifting Winds (>6m/s)	Snow Depth	Description
1	N	N	Constant	Quiet
2	N	Y	+ or -	Deposition or erosion
3	Y	N	+	Snowfall
4	Y	Y	+ or -	Deposition or erosion w/snowfall

Figures 45 and 46 are our preliminary attempts to identify the logical flow by which the conditions at C1 and E12 might be determined by software and the corrective actions that might then be implemented when the data diverge or need to be flagged as suspect. From left to right, the diagnostic variables used

are air temperature (obtainable from sonic depth sounders, LPMs, and SONICWIND3D), wind speed (obtainable from SONICWIND3D or the SPMFs), drift flux (SPMFs), snow depth (from the nine sonic depth sounders at each site), and precipitation intensities (LPMs). As the examples in the preceding section indicate, comparing the shielded to unshielded LPM potentially allows for identification of the component of the precipitation that has been lofted from snow deposited on the tundra. Settlement curves and dune migration are also diagnostics for erosion and deposition.

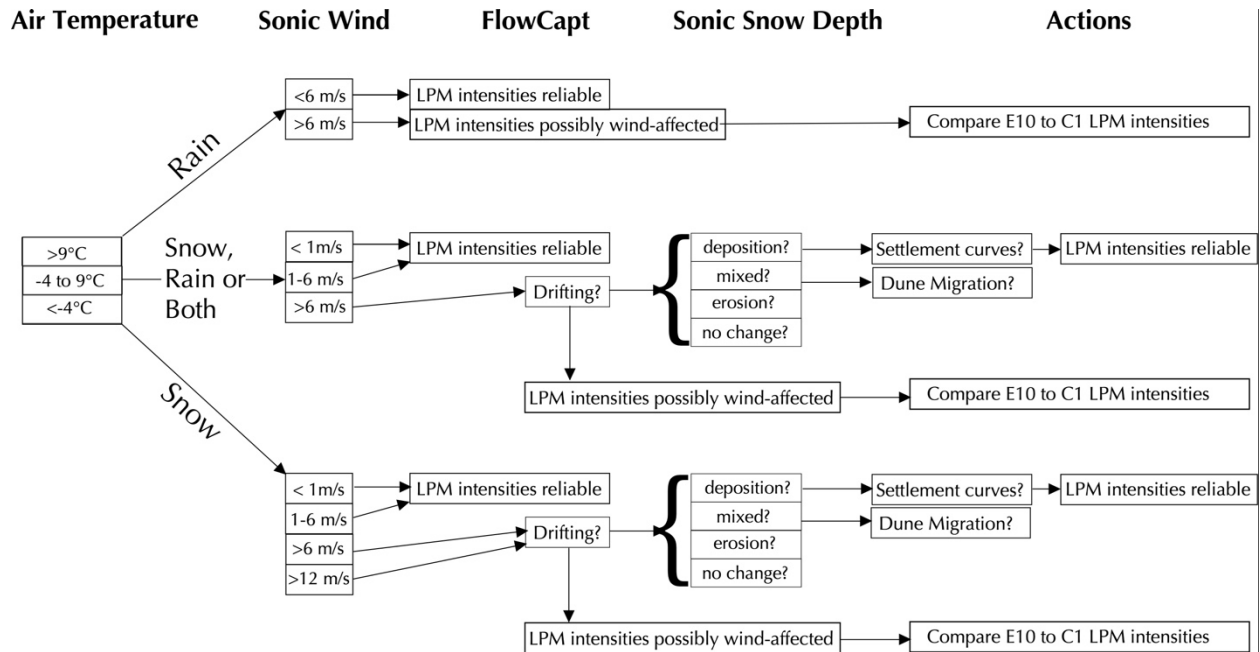


Figure 45. Flow chart suggesting how reliability of LPM data might be assessed.

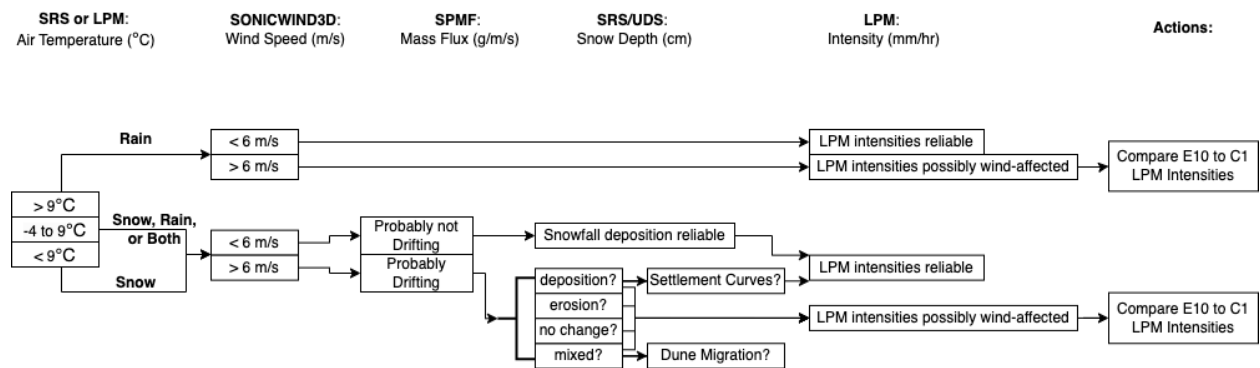


Figure 46. A simpler version of Figure 45 that might lend itself to easier implementation in code.

## 8.0 Conclusions

The arrays of instruments we have been operating at C1 and E12 provide a unique datastream for understanding the winter landscape evolution at Utqiaġvik as well as winter precipitation.

- An extensive set (18) of sonic depth sounders provides not only a useful mean snow depth, but also a measure of the range of snow depths as mediated by the hummocks and tussocks of the tundra. The full ensemble emphasizes the fact that one cannot simply use the mean depth alone, and certainly never the results from a single sensor. Variable micro-topography and high winds cause snow depths to vary across the polygonal landscape in predictable ways, and the array elucidates that depth-topography relationship.
- The Thies-Clima heated 3D sonic anemometer (or SONICWIND3D) functions flawlessly in a difficult environment and provides excellent high-resolution wind measurements. We think the heating is a critical feature in producing this high-quality record. Of particular value is the vertical wind, which can loft snow from the ground high enough to affect disdrometer measurements.
- A set of unique devices, the SPMFs, provide event monitoring of snow drifting, which has a major impact on the depth of the snow across the tundra and affects the results recorded by the LPM (precipitation) monitors. Without them, it would be difficult to know specifically when there was drifting snow, and the relative intensity of that drift. That is not a trivial result, as detecting blowing snow using other devices (like cameras or visibility sensors) is problematic.
- However, both calibration studies and local observations of the SPMFs indicate that they can greatly (by 50%) underestimate the total wind-blown flux. Potentially, using drifts captured by local snow fences near C1, it might be possible to empirically adjust the SPMF results through a calibration comparison procedure.
- The LPMs, while complex instruments, have the potential to give real insight into the type of precipitation taking place, as well as the amount. Using one shielded and one unshielded LPM may allow for correction when blowing snow from the tundra is entering the LPM count and biasing the results. If so, then more accurate winter precipitation intensities could be made.

Using each of these instruments in concert is vital in understanding what is happening in the tundra. Creating an algorithm that can use these datastreams to identify types of events is the next step in using these instruments. Table 7 and Figures 45 and 46 could provide a stepping stone for how we can automate and better use the data coming from the ARM snow arrays.

## 9.0 References

- Battaglia, A, E Rustemeier, A Tokay, U Blahak, and C Simmer. 2010. "PARSIVEL snow observations: A critical assessment." *Journal of Atmospheric and Oceanic Technology* 27(2): 333–344, <https://doi.org/10.1175/2009JTECHA1332.1>
- Bakkehoi, S, K Øien, and EJ Førland. 1985. "An automatic precipitation gauge based on vibrating-wire strain gauges." *Hydrology Research* 16(4): 193–202, <https://doi.org/10.2166/nh.1985.0015>
- Beard, KV, and C Chuang. 1987. "A new model for the equilibrium shape of raindrops." *Journal of the Atmospheric Sciences* 44(11): 1509–1524, [https://doi.org/10.1175/1520-0469\(1987\)044<1509:ANMFTE>2.0.CO;2](https://doi.org/10.1175/1520-0469(1987)044<1509:ANMFTE>2.0.CO;2)
- Bosio, R, A Cagninei, and D Poggi. 2023. "Large Laboratory Simulator of Natural Rainfall: From Drizzle to Storms." *Water* 15(12): 2205, <https://doi.org/10.3390/w15122205>

- Campbell Scientific. 2016. Instruction Manual for the SR50A, SR50A-316SS, and SR50AH Sonic Ranging Sensors, Revision: 10/16, <https://s.campbellsci.com/documents/cr/manuals/sr50a.pdf>
- Cornish, V. 1902. “On snow-waves and snow-drifts in Canada, with notes on the “snow-mushrooms” of the Selkirk Mountains.” *The Geographical Journal* 20(2): 137–173.
- Doumani, GA. 1966. “Surface structures in snow.” *International Conference on Low Temperature Science, vol. 1, Physics of Snow and Ice*, 1119–1136, Hokkaido University, Hokkaido, Japan.
- Duchon, CE. 2008. “Using vibrating-wire technology for precipitation measurements.” In *Precipitation: Advances in Measurement, Estimation and Prediction*, 33–58. Berlin, Heidelberg: Springer Berlin Heidelberg, [https://doi.org/10.1007/978-3-540-77655-0\\_2](https://doi.org/10.1007/978-3-540-77655-0_2)
- Fehlmann, M, M Rohrer, A von Lerber, and M Stoffel. 2020. “Automated precipitation monitoring with the Thies disdrometer: biases and ways for improvement.” *Atmospheric Measurement Techniques* 13(9): 1–31, <https://doi.org/10.5194/amt-13-4683-2020>
- Filhol, S, and M Sturm. 2019. “The smoothing of landscapes during snowfall with no wind.” *Journal of Glaciology* 65(250): 173–187, <https://doi.org/10.1017/jog.2018.104>
- Gorgucci, E, I Baldini, and V Chandrasekar. 2006. “What is the shape of a raindrop? An answer from radar measurements.” *Journal of the Atmospheric Sciences* 63(11): 3033–3044, <https://doi.org/10.1175/JAS3781.1>
- Gunn, R, and GD Kinzer. 1949. “The terminal velocity of fall for water droplets in stagnant air.” *Journal of the Atmospheric Sciences* 6(4): 243–248, [https://doi.org/10.1175/1520-0469\(1949\)006<0243:TTVOFF>2.0.CO;2](https://doi.org/10.1175/1520-0469(1949)006<0243:TTVOFF>2.0.CO;2)
- Kojima, K. 1967. “Densification of seasonal snow cover.” *International Conference on Low Temperature Science, vol. 1, Physics of Snow and Ice: Proceedings 1(2)*:929–952, Hokkaido University, Hokkaido, Japan.
- Kochanski, K, RS Anderson, and GE Tucker. 2019. “The evolution of snow bedforms in the Colorado Front Range and the processes that shape them.” *The Cryosphere* 13(4): 1267–1281, <https://doi.org/10.5194/tc-13-1267-2019>
- Kochendorfer, J, R Rasmussen, M Wolff, B Baker, ME Hall, T Meyers, S Landolt, A Jachcik, K Isaksen, R Braekkan, and R Leeper. 2017. “The quantification and correction of wind-induced precipitation measurement errors.” *Hydrology and Earth System Sciences* 21(4): 1973–1989, <https://doi.org/10.5194/hess-21-1973-2017>
- Li, L, and JW Pomeroy. 1997. “Estimates of threshold wind speeds for snow transport using meteorological data.” *Journal of Applied Meteorology and Climatology* 36(3): 205–213, [https://doi.org/10.1175/1520-0450\(1997\)036<0205:EOTWSF>2.0.CO;2](https://doi.org/10.1175/1520-0450(1997)036<0205:EOTWSF>2.0.CO;2)
- Löffler-Mang, M, and J Joss. 2000. “An optical disdrometer for measuring size and velocity of hydrometeors.” *Journal of Atmospheric and Oceanic Technology* 17(2): 130–139, [https://doi.org/10.1175/1520-0426\(2000\)017<0130:AODFMS>2.0.CO;2](https://doi.org/10.1175/1520-0426(2000)017<0130:AODFMS>2.0.CO;2)

- McDonald, JE. 1954. “The shape and aerodynamics of large raindrops.” *Journal of the Atmospheric Sciences* 11(6): 478–494, [https://doi.org/10.1175/1520-0469\(1954\)011<0478:TSAAOL>2.0.CO;2](https://doi.org/10.1175/1520-0469(1954)011<0478:TSAAOL>2.0.CO;2)
- Mitchell, DL, R Zhang, and RL Pitter. 1990. “Mass-dimensional relationships for ice particles and the influence of riming on snowfall rates.” *Journal of Applied Meteorology and Climatology* 29(2): 153–163, [https://doi.org/10.1175/1520-0450\(1990\)029<0153:MDRFIP>2.0.CO;2](https://doi.org/10.1175/1520-0450(1990)029<0153:MDRFIP>2.0.CO;2)
- North Dakota State University. 2024. Fargo North Dakota Annual Wind Speed Average Data. [https://www.ndsu.edu/climate/North%20Dakota%20Data/Yearly%20Wind%20Avg/Fargo\\_County\\_North\\_Dakota.html](https://www.ndsu.edu/climate/North%20Dakota%20Data/Yearly%20Wind%20Avg/Fargo_County_North_Dakota.html)
- Redilla, K, ST Pearl, PA Bieniek, and JE Walsh. 2019. “Wind climatology for Alaska: historical and future.” *Atmospheric and Climate Sciences* 9(4), <https://doi.org/10.4236/acs.2019.94042>
- Sturm, M, and J Holmgren. 1998. “Differences in compaction behavior of three climate classes of snow.” *Annals of Glaciology* 26: 125–130, <https://doi.org/10.3189/1998AoG26-1-125-130>
- Sturm, M, and C Benson. 2004. “Scales of spatial heterogeneity for perennial and seasonal snow layers.” *Annals of Glaciology* 38: 253–260, <https://doi.org/10.3189/172756404781815112>
- Sturm, M, and S Stuefer. 2013. “Wind-blown flux rates derived from drifts at arctic snow fences.” *Journal of Glaciology* 59(213): 21–34, <https://doi.org/10.3189/2013JoG12J110>
- Sturm, M, and J Holmgren. 2018. “An automatic snow depth probe for field validation campaigns.” *Water Resources Research* 54(11): 9695–9701, <https://doi.org/10.1029/2018WR023559>
- Tabler, RD. 1994. *Design guidelines for the control of blowing and drifting snow* (Vol. 364). Washington, D.C.: Strategic Highway Research Program, National Research Council. <https://onlinepubs.trb.org/onlinepubs/shrp/SHRP-H-381.pdf>
- Thies-Clima 2008. Laser Precipitation Monitor 5.4110.xx.x00 V2.4x STD: Instructions for Use. 021341/08/07, [https://www.thiesclima.com/db/dnl/5.4110.xx.x00\\_Laser\\_Precipitation\\_Monitor\\_eng.pdf](https://www.thiesclima.com/db/dnl/5.4110.xx.x00_Laser_Precipitation_Monitor_eng.pdf)
- Trouvilliez, A, F Naaim-Bouvet, H Bellot, C Genthon, and H Gallée. 2015. “Evaluation of the SPMF acoustic sensor for the aeolian transport of snow.” *Journal of Atmospheric and Oceanic Technology* 32(9): 1630–1641, <https://doi.org/10.1175/JTECH-D-14-00104.1>
- Vázquez-Martín, S, T Kuhn, and S Eliasson. 2021a. “Mass of different snow crystal shapes derived from fall speed measurements.” *Atmospheric Chemistry and Physics* 21(24): 18669–18688, <https://doi.org/10.5194/acp-21-18669-2021>
- Vázquez-Martín, S, T Kuhn, and S Eliasson. 2021b. “Shape dependence of snow crystal fall speed.” *Atmospheric Chemistry and Physics* 21(10): 7545–7565, <https://doi.org/10.5194/acp-21-7545-2021>
- Washburn, AL. 1956. “Classification of patterned ground and review of suggested origins.” *Geological Society of America Bulletin* 67(7): 823–866, [https://doi.org/10.1130/0016-7606\(1956\)67\[823:COPGAR\]2.0.C\);2](https://doi.org/10.1130/0016-7606(1956)67[823:COPGAR]2.0.C);2)

## Appendix A

### Modifications of Data Prior to Ingest (A1) Level

The data from the instruments described above can be found at the ARM Data Center web interface (<https://adc.arm.gov/discovery/#/>). There are a few minimal but important data processing steps that happen in producing the A1-level data there and which can be downloaded as NetCDF files.

#### A.1 Sonic Ranging Sounders (SRSs)

The SRSs measure the distance from the ground via an ultrasonic ping. Depending on the ambient temperature, the speed of that ping varies, and to produce this correction, we measure and archive the air temperature near the sounders. This variable speed is accounted for using the equation in Section 2.0 when the data are ingested from our data loggers into the ARM Data Center. The raw results are also stored along with the air temperatures.

## Appendix B

### “A1+”-Level Data Processing

Appendix B addresses data processing steps we have used for each instrument to use the data sets for analysis. Some processing steps were universal to each instrument, and some were specific to one. This A1+ level of data processing was used for our exploratory data analyses described in this document.

#### B.1 Universal Data Level Processing

Figure 47 is a chart representing the data processing workflow we created in Python.

##### ARM A1+ Level Processing

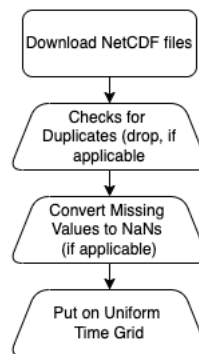


**Figure 47.** Flow chart of our A1+ data processing.

After acquisition of an instrument’s data, we load the NetCDF data files into Python using the ARM Atmospheric data Community Toolkit module (<https://github.com/ARM-DOE/ACT>). In this processing, we check for duplicate timestamp data and keep the first reading, which is not typical but can occasionally occur, depending on the ARM datastream (however, this did not occur with our instrument datastreams). We then check for and replace missing values defined by the NetCDF files; these are labeled at the -9999 value, with *NaNs* (again, however, we did not find any in our check). Finally, we put the data on a uniform time grid for both the 1-minute and 10-second sampling instruments and fill missing dates with *NaNs*.

## B.2 Instrument-Specific Data Level Processing

### B.2.1 SRS

The primary A1+-level data processing for the SRSs is converting the distance measured to the ground using an ultrasonic ping to a useful depth value. To convert these values to snow depth we need to convert the distance to a depth using Equation [1] from Section 2.0. For our exploratory data analysis, we visually estimated this no-snow value using IGOR Pro software (<https://www.wavemetrics.com/>). However, if using Python, this estimate can be done by simply taking the average of the distance readings of the summer months. We tested this using an average of all July and August minute readings and retrieved a useful value as well. After the conversion, as stated in Section 2.0, we applied an upper and lower threshold to filter out erroneous data as well as smoothed the minute data using a rolling average of 60-minute intervals.

### B.2.2 SONICWIND3D

Presently, the only significant data set processing we do, other than manipulation of the format of the data, is generating new variables for SONICWIND3D. These are the horizontal magnitude of the wind speed and its azimuthal direction. They are generated using these Python functions made using the NumPy library:

```
# u_wind: Eastward wind component
# v_wind: Northward wind component
# w_wind: Vertical wind component
def compute_azimuth(x_wind, y_wind):
    x_wind = np.array(x_wind)
    y_wind = np.array(y_wind)
    n_horiz_azm = np.zeros(len(x_wind))
    for i in range(len(x_wind)):
        n_horiz_azm[i] = (90 if x_wind[i] >= 0 else 270) - (np.arctan(y_wind[i]/x_wind[i]) * (180/(np.pi)))
    return n_horiz_azm

def compute_horizontal_speed(x_wind, y_wind):
    x_wind = np.array(x_wind)
    y_wind = np.array(y_wind)
    horiz_spd = np.sqrt(x_wind**2 + y_wind**2)
    return horiz_spd
```



[www.arm.gov](http://www.arm.gov)

U.S. DEPARTMENT OF  
**ENERGY**

---

Office of Science